

# Advance in Close-Edged Graphene Nanoribbon: Property Investigation and Structure Fabrication

Maoshuai He,\* Jichen Dong, Haomin Wang, Han Xue, Qianru Wu, Benwu Xin, Wenke Gao, Xiaolong He, Jin Yu, Haidong Sun, Feng Ding, and Jin Zhang\*

The absence of dangling bonds in close-edged graphene nanoribbons (CEGNRs) confers upon them a series of fascinating properties, especially when compared with cylindrical carbon nanotubes and open-edged GNRs. Here, the configuration of CEGNRs is described, followed by the structure-related properties, including mechanical, thermal, electrical, optical, and magnetic properties. Based on the unique structures and extraordinary properties, their potential applications in a variety of fields, such as field-effect transistors, energy suppliers, nanoactuators, and fibers, are discussed. Remarkably, the strategies applied for generating CEGNRs, mainly from the collapse of carbon nanotubes and graphene tubes, are depicted in detail. Finally, the prospects in the research area of CEGNRs are proposed.

## 1. Introduction

The landmark work of Novoselov et al.<sup>[1]</sup> has brought graphene to the worldwide attention. Owing to its unique structure, graphene exhibits remarkable mechanical, thermal, and electrical properties.<sup>[2]</sup> It is a promising interconnect material in replacing fragile copper in modern computer microchips and robust against short-channel effects down to very short gate lengths.<sup>[3]</sup> Unfortunately, its application in transistor devices is inhibited by the zero-energy bandgap. Consequently, different strategies, such as substrate inducing,<sup>[4]</sup> patterned adsorption of atomic hydrogen,<sup>[5]</sup> chemical functionalization and doping,<sup>[6]</sup> have been developed to

open energy gaps in graphene. Most of the processes inevitably destroy the pristine structure of graphene, causing a significant degradation in electron mobility.<sup>[7]</sup>

Alternatively, electronic confinement of graphene in one in-plane direction is proposed to open a bandgap without affecting the mobility dramatically, promoting the thriving of the graphene nanoribbons (GNRs).<sup>[8]</sup> Using a tight binding model, Wakabayashi et al.<sup>[8b]</sup> revealed that the energy bandgap is inversely proportional to the ribbon width, as later verified experimentally.<sup>[8c,9]</sup> A number of approaches, including chemical vapor deposition (CVD),<sup>[10]</sup> epitaxial precipitation,<sup>[11]</sup> nanotomy,<sup>[12]</sup> and organic chemical method,<sup>[13]</sup> have been developed to synthesize GNRs.<sup>[14]</sup> The produced GNRs having dangling bonds particularly in the major axial direction are defined as open-edged GNRs. However, most of them suffer disordered edges, making the bandgap of GNR poorly defined.<sup>[8c,11,15]</sup>

Different from open-edged ones, GNRs without dangling bonds in the long axial direction are defined as close-edged GNRs (CEGNRs).<sup>[16]</sup> The configuration of a CEGNR resembles that of a collapsed carbon nanotube (CNT). Indeed, collapse of CNTs or graphene nanotubes leads to the formation of CEGNRs,<sup>[16b,d]</sup> providing a facile route for their fabrication. Pioneering work on studying collapsed carbon nanotubes was reported by Chopra et al.,<sup>[16a]</sup> who observed the flattened CNTs using transmission electron microscopy (TEM). Under certain conditions, collapsed CNTs are energetically favored over inflated counterparts.<sup>[16a]</sup> Since then, a surge of interest in collapsed CNTs has occurred in a number of disciplines, including determination of the threshold CNT diameter,<sup>[16b,d,17]</sup> property investigation,<sup>[18]</sup> and application seeking.<sup>[19]</sup> However, the

Prof. M. He

Key Laboratory of Eco-Chemical Engineering  
Ministry of Education

Taishan Scholar Advantage and Characteristic Discipline

Team of Eco Chemical Process and Technology

College of Chemistry and Molecular Engineering

Qingdao University of Science and Technology

Qingdao 266042, China

E-mail: hemaoshuai@qust.edu.cn

Prof. M. He, H. Wang, H. Xue, Q. Wu, B. Xin, W. Gao,

X. He, J. Yu, H. Sun

School of Materials Science and Engineering

Shandong University of Science and Technology

Qingdao 266590, China

Dr. J. Dong, Prof. F. Ding

Center for Multidimensional Carbon Materials

Institute for Basic Science

UNIST-gil 50, Ulsu-gun, Ulsan 44919, South Korea

Prof. F. Ding

School of Materials Science and Engineering

Ulsan National Institute of Science and Technology

Ulsan 44919, South Korea

Prof. J. Zhang

Center for Nanochemistry

Beijing Science and Engineering Center for Nanocarbons

Beijing National Laboratory for Molecular Sciences

Key Laboratory for the Physics and Chemistry of Nanodevices

College of Chemistry and Molecular Engineering

Peking University

Beijing 100871, China

E-mail: jinzhang@pku.edu.cn

 The ORCID identification number(s) for the author(s) of this article can be found under <https://doi.org/10.1002/sml.201804473>.

DOI: 10.1002/sml.201804473

dearth of experimental studies raises difficulties in obtaining a convergent result. Besides, although several review articles have been dictated to graphene and graphitic nanoribbon,<sup>[14c,20]</sup> a comprehensive review on CEGNRs is lacking.

In this review, we will first clarify the structure of CEGNRs. Based on its extraordinary structures, the properties and the potential applications of CEGNRs are addressed (Figure 1). Subsequently, different approaches applied for preparing collapsed CNTs are described. Particularly, the spontaneous collapse of CNTs toward the formation of CEGNRs is investigated extensively and the efforts in determining threshold diameter for CNT collapse are described. Finally, the challenges existing in CEGNR research and the prospects are proposed.

## 2. Fundamentals of CEGNRs

### 2.1. Structure of CEGNRs

We start the description of CEGNR structure with CNT configuration. A single-walled carbon nanotube (SWNT) can be viewed as a cylindrically roll-up a graphene sheet (Figure 2a),<sup>[21]</sup> and has been widely investigated in the past two decades.<sup>[22]</sup> Under suitable conditions, SWNT tends to adopt a collapsed configuration, consisting of two highly strained circular edges bridged by a flat middle section (Figure 2b).<sup>[16b,17,19a,23]</sup> Such a configuration is stabilized by the van der Waals (vdW) interaction between two opposite walls.<sup>[21]</sup> In either edge, there is a highly strained bulb (or circular edge) with a calculated height ranging from 0.46 to 1.07 nm.<sup>[24]</sup> The height of the edge is sensitive to many factors, such as tube diameter, chirality, the presence of substrate, etc.<sup>[16b,d]</sup> When a SWNT is situated on substrate<sup>[25]</sup> or bundled with other tube,<sup>[26]</sup> the strained bulbs just bulge one side (Figure 2c,d).

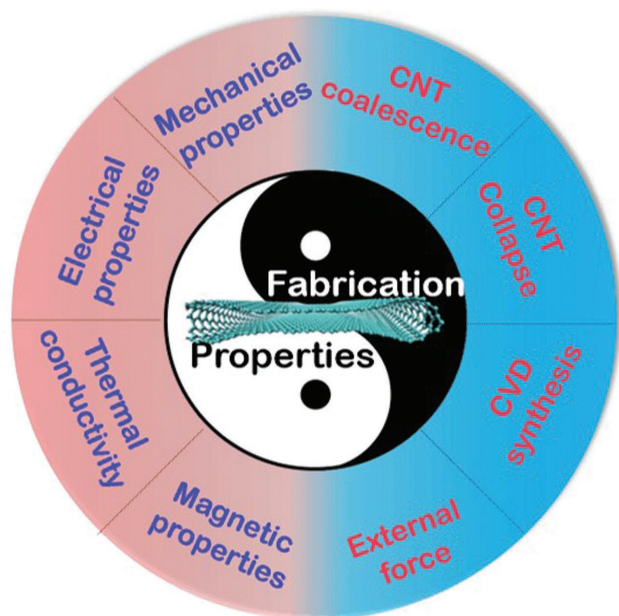


**Figure 1.** The properties of CEGNRs and the strategies applied for fabricating them.



**Maoshuai He** received his Ph.D. degree in chemistry from the Peking University in 2006. After working as a post-doctoral fellow in the Centre National de la Recherche Scientifique (CNRS) in France and the Aalto University in Finland, he joined the Shandong University of Science and Technology in 2016. In 2018, he moved to

the Qingdao University of Science and Technology. His research is focused on controlled synthesis and applications of carbon nanomaterials.



**Jin Zhang** received his PhD from the Lanzhou University in 1997. After a two-year postdoctoral fellowship at the University of Leeds, UK, he returned to the Peking University where he was appointed Associate Professor (2000) and promoted to Full Professor in 2006. In 2013, he was appointed as Changjiang professor.

He also is a Fellow of the RSC. His research focuses on the controlled synthesis and spectroscopic characterization of carbon nanomaterials.

Similar to SWNTs, multiwall carbon nanotubes (MWNTs) also possess two equilibrium states (Figure 2e,f).<sup>[23,27]</sup> In the collapsed state, the distance between flat layers is near 0.34 nm, leading to a constant perimeter difference between successive layers.<sup>[17]</sup> With the increase of wall numbers, the inner wall bulb radius decreases and the height ratio between the edge and the flat part approaches to 1 (Figure 2f).<sup>[27]</sup> Upon collapse, the curvature energies of all the walls increase and only the inner wall gains attractive vdW energy.

### 2.2. Properties of CEGNRs

Most CEGNRs are produced from the collapse of CNTs. Such a collapse susceptibility originates from the flexibility of the graphene sheets in bending, and ultimately affects the properties of the CEGNRs.

#### 2.2.1. Mechanical Properties

CNTs demonstrate high tensile strength and large Young's modulus in the axial direction.<sup>[28]</sup> After collapse from the radial direction, the mechanical properties in the axial direction are inherited. Moreover, collapsed CNTs exhibit a higher flexibility

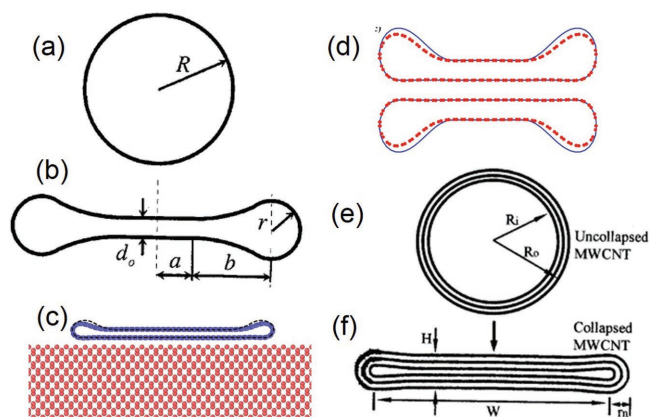


**Figure 2.** The possible configurations for: a) a circular SWNT; b) a collapsed configuration with interplanar distance of  $d_0$ . Reproduced with permission.<sup>[21]</sup> Copyright 2005, American Institute of Physics; c) a collapsed SWNT on substrate; d) collapsed SWNT bundle. Reproduced with permission.<sup>[25b]</sup> Copyright 2013, IOP Publishing Ltd.; e) a cylindrical and f) a fully collapsed MWNT. Reproduced with permission.<sup>[27]</sup> Copyright 2001, American Institute of Physics.

than the inflated counterparts.<sup>[27]</sup> **Figure 3a** presents an atomic force microscopy (AFM) image of dispersed CNTs on silicon wafer surface. A close-up view of the segment demonstrates a “pillow-”like configuration (Figure 3b), a characteristic of collapsed CNT. Its section analysis (Figure 3c) indicates that the collapsed CNT has a height of 3.1 nm and a width of 30 nm. Figure 3d depicts the 3D images of the collapsed CNT, which

closely follows the contour of the underlying CNT, indicating a high flexibility. By contrast, cylindrical CNTs do not exhibit such a flexibility when crossing other CNTs or surface contaminations.

Besides the high flexibility, the collapsed CNTs have stronger interactions with adjacent CNTs in bundles, rendering fibers with superior mechanical properties.<sup>[19a,29]</sup> Zhang et al.<sup>[26]</sup> studied adhesion between two identical, radially collapsed CNTs and compared the energy with that of cylindrical and deformed CNTs. Figure 3e shows the three types of configurations for two CNTs. The adhesion energies as a function of CNT diameter for the three configurations are calculated (Figure 3f). Clearly, the collapsed configuration has much larger adhesion energy than the other two cases. Experimentally, Motta et al.<sup>[19a]</sup> directly spun fibers out of a CVD reaction zone which consist of bundled CNTs with “dog bone” configuration (Figure 3g). The stress–strain curves of the fibers give an average strength of  $1.1 \text{ N tex}^{-1}$  and a stiffness of  $60 \text{ N tex}^{-1}$  (Figure 3h). The high mechanical performance of the fiber arises from the stress transfer in shear between neighboring CNTs. The high flexibility and superior mechanical properties of collapsed CNTs are necessary for developing high performance fibers.

### 2.2.2. Thermal Conductivities

All CNTs are supposed to be good thermal conductors along the axial direction. An individual SWNT could demonstrate a thermal conductivity of  $3500 \text{ W m}^{-1} \text{ K}^{-1}$  at room temperature,<sup>[30]</sup> which is comparable with that of diamond. Such a high thermal

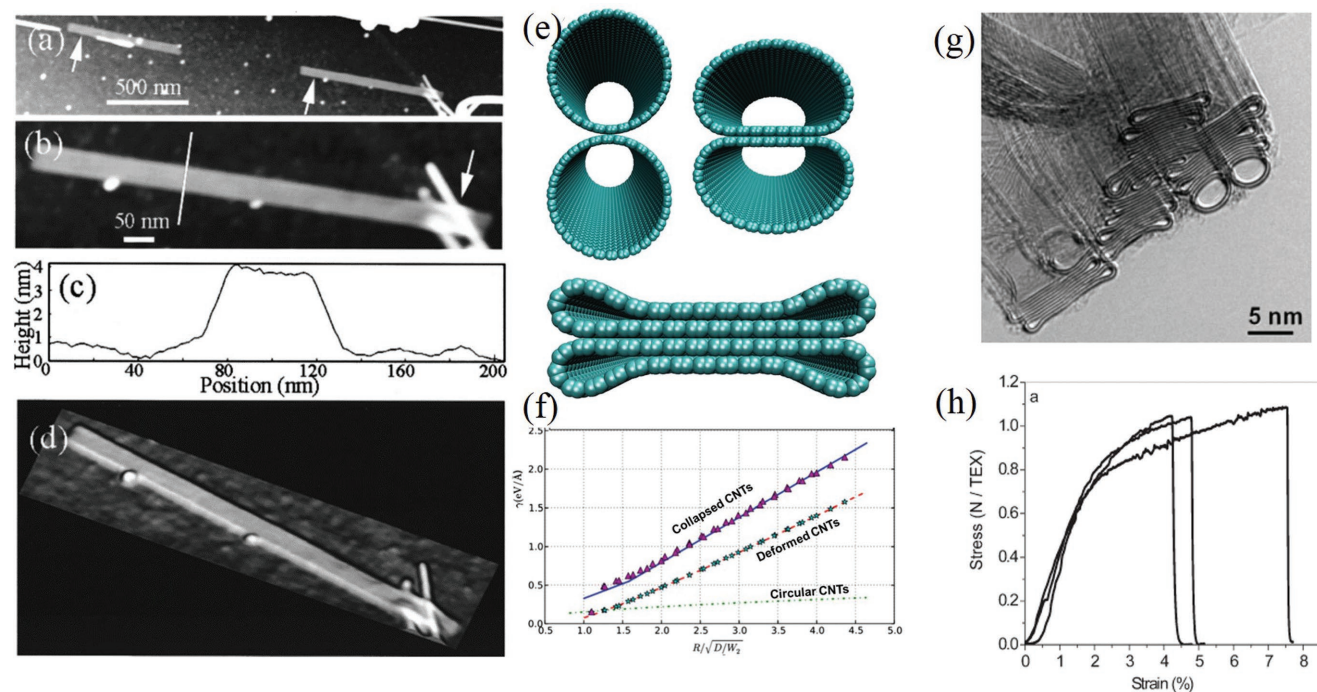


**Figure 3.** a) AFM image of two collapsed CNTs with flattened configuration. b) A close-up image of the collapsed CNT. c) Height analysis of the tube. d) 3D image of the CEGNR.<sup>[27]</sup> Reproduced with permission. Copyright 2001, American Institute of Physics. e) Three types of configurations with two identical SWNTs: cylindrical, deformed, and collapsed ones. f) Comparison of the adhesion energy as a function of the SWNT diameter for the three configurations. Reproduced with permission.<sup>[26]</sup> Copyright 2013, Springer-Verlag Wien. g) TEM image of the CNTs with “dog bone” configuration. h) Stress–strain curves of three fibers consisted of collapsed CNTs. Reproduced with permission.<sup>[19a]</sup> Copyright 2007, Wiley-VCH.

conductivity is attributed to the large phonon mean free path of CNTs. Using nonequilibrium molecular dynamics (MD), Al-Ghalith et al.<sup>[31]</sup> recently compared the thermal transport of cylindrical and collapsed CNTs. Figure 4a,b describes the setup applied for the  $\kappa$  calculations. The heat flux along a CNT is estimated by the different rates of the kinetic energy extraction from the two reservoirs. To calculate the interfacial thermal resistance of collapsed CNTs, heat baths are applied on the left and the right CNT in the stack (Figure 4c).

SWNT exhibits strong ballistic behavior over sub-micrometer length scales.<sup>[32]</sup> Figure 4d (filled symbols) presents the calculated  $\kappa$  for a circular (50, 50) SWNT as a function of tube length.<sup>[31]</sup> The initial linear increase indicates a pure ballistic behavior, i.e., phonons propagate without being scattered. With increasing SWNT length (above  $\approx 200$  nm), more phonon modes with longer wavelengths are supported, contributing to the increase of  $\kappa$  in the diffusive regime. Upon collapse, the formation of a vdW bilayer with two strained edge bulbs has impact on the  $\kappa$ , although the ballistic transport is not affected. As shown in Figure 4d (empty symbol), a smaller  $\kappa$  than that of cylindrical CNT is observed in the diffusive regime. The result indicates that the heat carrying phonons scatter more effectively in the collapsed CNTs. The cross-sectional collapse-induced small reduction of  $\kappa$  is caused by the slight increase of radial-breathing transverse acoustic phonon scattering through the anharmonicity. Remarkably, the strained edges connect the bilayer in a way that limits the cross-plane scattering, which does not reduce the  $\kappa$  in the CEGNRs. By contrast, the rough edges in open-edged GNRs can perturb phonon propagation and therefore significantly reduce  $\kappa$ . Figure 4e compares the  $\kappa$  of collapsed (30, 30) CNTs with that of open-edged bilayer GNRs. Different from collapsed CNTs, the GNRs with rough edges display diffusive phonon scattering. An  $\approx 83\%$  reduction

in  $\kappa$  is calculated for the longest GNR with open edges. The results highlight the importance of closed edges in inheriting the high  $\kappa$  of their parent cylindrical counterparts.

Although the  $\kappa$  of collapsed CNTs is slightly lower than that of cylindrical CNTs, when they are tightly packed, the interfacial thermal resistance between collapsed CNTs ( $9.69 \times 10^9$  K W<sup>-1</sup>) is much smaller than that between cylindrical CNTs ( $2.38 \times 10^{10}$  K W<sup>-1</sup>). The small interfacial thermal resistance is owing to the larger number of carbon atoms in effective vdW contact between collapsed CNTs (Figure 4c).<sup>[31]</sup> Therefore, aligned, long CNTs in stacked, collapsed architectures are promising for efficient heat transport in lightweight composite materials.

### 2.2.3. Electrical Properties

The electronic structure evolutions of CNTs upon radial deformation have been calculated.<sup>[33]</sup> By the creation of inhomogeneous curvature and the introduction of coupling between interior faces, the collapse changes the electronic structure of SWNT. For example, Lammert et al.<sup>[33b]</sup> calculated the band structures of the collapsed SWNTs with different chiralities. The interlayer coupling governs the low-energy electronic properties in an energy range from 0.1 to 0.2 eV. Upon collapse, ( $n, n$ ) metallic CNTs become semiconducting and ( $3n, 0$ ) species with small curvature-induced gaps become gapless. Through first-principle calculations, Mazzoni and Chacham<sup>[33a]</sup> investigated the effect of flattening on the electronic properties of a semiconducting CNT. The cross-section flattening causes a progressive reduction of the bandgap, leading to a semiconductor–metal transition. Despite the great efforts in computer simulations, the overall conclusions on the evolution of the electrical properties of CNTs upon collapse are at odds.

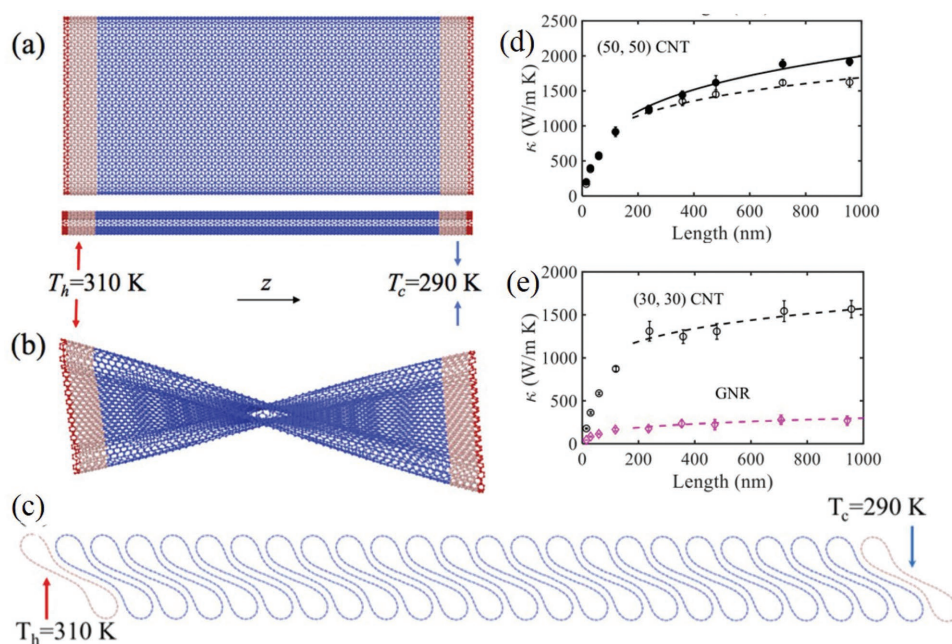


**Figure 4.** Nonequilibrium MD setup for collapsed CNTs: a) a straight one; b) a twisted one. c) Nonequilibrium MD setup for computing the intertube thermal resistance in a stack of collapsed CNTs. d)  $\kappa$  of a cylindrical (filled symbols) and a collapsed (empty symbols) (50, 50) CNT. e) Comparison of  $\kappa$  in a collapsed (30, 30) CNT and a two-layer GNR with similar width but rough edges. Reproduced with permission.<sup>[31]</sup> Copyright 2017, American Physical Society.

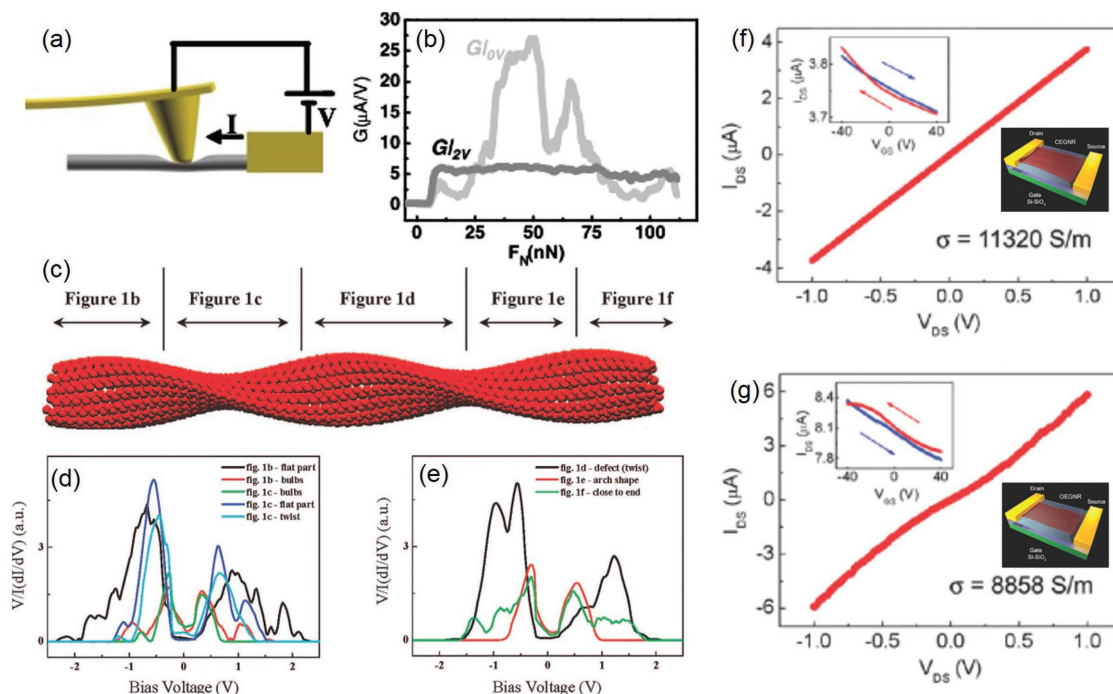


**Figure 5.** a) Schematic illustration of setup for deforming CNT and measuring CNT conductance. b) Plot of the conductance as a function of cantilever normal force. Reproduced with permission.<sup>[34]</sup> Copyright 2006, American Physical Society. c) Schematic model of a collapsed CNT, mimicking the configuration of an investigated CNT by scanning electron microscopy. d,e) Scanning tunneling spectroscopy spectra recorded on the collapsed nanotube at different positions. Reproduced with permission.<sup>[18]</sup> Copyright 2008, American Chemical Society. Conductivity measurement of f) CEGNR and g) open-edged GNR. Insets show the schematic illustration of GNR field-effect transistors and their transfer characteristics. Reproduced with permission.<sup>[37]</sup> Copyright 2010, American Chemical Society.

Experimentally, the electronic structures of deformed CNTs was investigated by employing a novel setup (Figure 5a) which allows direct probing of the local electronic properties of CNTs while they are deformed.<sup>[34]</sup> In the setup, the AFM tip serves both as an electrode and to induce local deformation. Figure 5b displays a plot of the conductance ( $G$ ) as a function of the cantilever force ( $F_N$ ). In the range of low-loading force, the conductance measured at 0 V ( $G_{|0V}$ ) increases with the loading force, which is related to the electrical contact improvement.<sup>[35]</sup> Further increasing the  $F_N$  over 50 nN leads to the drop of  $G$ , indicating the opening of a bandgap by radial deformation. A localized semiconductor-to-metal transition of SWNT upon deformation was recently explored by Raman spectroscopy,<sup>[36]</sup> where the Fano interaction in the  $G$  mode is adopted as an indication of metallic behavior. By analyzing the deconvoluted components of  $G$  band along CNT length, it is revealed that physical distortion could locally modify the electronic properties of CNT within a length smaller than 15 nm.

The abovementioned experiments are focused on CNTs undergoing mechanical deformation, which represents only a unit of collapsed CNT. Using scanning tunneling microscopy and spectroscopy, Giusca et al. compared the electronic structures at different spots of a collapsed CNT (Figure 5c).<sup>[18]</sup> The normalized differential conductance,  $V/I(dI/dV)$ , provides a good measure of the local density of states (DOS), the spectra of which acquired at different locations of the CNT are presented in Figure 5d,e. The undeformed tube shows a positive and finite DOS at the Fermi energy, a typical of metallic behavior. The data recorded

on the flat part of the collapsed CNT demonstrate zero DOS at the Fermi energy between  $-0.2$  and  $+0.2$  V, corresponding to a semiconductor. Unlike the central flat part, the strained bulbs at the edges of the collapsed CNT show a finite DOS in the tunneling spectra, resembling the spectra of the undeformed CNT. To wrap all this up, the radial deformation in collapsed CNTs could modify the bandgap, which is crucial at metal contacts and has important implication in fabricating multiple quantum dots.

Besides the modification of bandgap, the electrical conductivity of CNT could increase upon deformation. Balima et al. investigated the conductivities of MWNs in a polyamide matrix as a function of applied pressure.<sup>[38]</sup> The high pressure would induce a radial collapse of CNTs, leading to a resistance reduction and a better junction transmission. Similarly, CEGNRs obtained from graphene tube collapse also demonstrate superior conductivity, especially when compared with open-edged GNRs (Figure 5f,g).<sup>[37]</sup> The improved conductivity of CEGNRs is attributed to the reduced parasitic defects at the edge region in CEGNRs.

#### 2.2.4. Optical and Magnetic Properties

The electronic structures of collapsed CNTs, i.e., CEGNRs could also be reflected by their optical properties. Optical adsorption of collapsed CNTs was calculated for different electric field configurations of incident light and described by dynamical conductivity for the polarization of electric field parallel to the axis.<sup>[39]</sup> Clear interband peaks corresponding

to bandgaps between allowed bands appear. Meanwhile, collapse-induced interwall interaction leads to splitting and shift of the peaks. The overall effect is sensitive to CNT chirality: achiral CNTs have relative large displacement of two layers in the flattened region and therefore large effect; while the effect is minor for chiral CNTs, which have negligible displacement upon collapse.<sup>[39]</sup> Besides CNT chirality, wall number also affects the optical properties of collapsed CNTs. By combining a classical force field model, a tight-binding model, and first-principle calculations, Yang and Wu<sup>[40]</sup> compared the optical properties of cylindrical and collapsed double-walled CNTs. After collapse, their optical properties change dramatically, and a strong anisotropy appears in the collapsed structure.

The orbital magnetic susceptibility of collapsed CNTs was calculated within an effective-mass scheme for two magnetic-field configurations, perpendicular and parallel to the flattened plane.<sup>[41]</sup> The response is diamagnetic in both the directions, and much larger in the perpendicular direction. The magnetic susceptibility modification upon collapse arises from the relatively large displacement of two layers in the flattened region. Consequently, the susceptibility is strongly modified in collapsed achiral CNTs and the modification is very small in collapsed chiral CNTs.<sup>[8b]</sup>

### 2.3. Applications of CEGNRs

The properties of CEGNRs arise from their unique configuration. CEGNRs with identical structures would exhibit same properties. Together with the lack of dangling bonds, CEGNRs

are expected to demonstrate properties with long-term stability and be potentially applied in many fields. Like other GNRs,<sup>[20a]</sup> the imminent applications of CEGNRs are in electronics such as the fabrication of ultrafast transistors, sensors, nano-electromechanical systems, highly conducting transparent films, etc. The generation of bandgap in CEGNRs renders them a promising component in field-effect transistor (FET). Martel et al.<sup>[42]</sup> compared the FETs made of tubular MWNTs and collapsed CNTs. MWNTs with relatively large diameter demonstrate metal character and no gate action (curve A of **Figure 6a**). A bandgap is generated in collapsed MWNT and it shows a significant gate effect (curve B in **Figure 6a**). Clearly, the source–drain current of the FET increases with increasing gate voltage, indicating that the dominant conduction process is hole transport.

Taking the advantage of successive collapse into CEGNRs, Chang<sup>[43]</sup> proposed an energy supplier based on domino wave generated along the longitudinal direction. From the MD simulations, once a section of a CNT with appropriate diameter is collapsed, the neighboring portions can collapse and produce a domino wave which can accelerate and finally shoot out the molecules inside CNT.<sup>[43a]</sup> **Figure 6b** presents the change of total system potential energy as a function of time during CNT collapse. Remarkably, the middle region (A → B) is correlated with the domino process. During the process, the vdW potential energy stored in CNT is partly converted into kinetic energy which keeps the propagation of domino wave. A temperature-induced reversible dominos in CNTs is also proposed.<sup>[43b]</sup> For a CNT with only one collapsed end, the collapse zone spreads

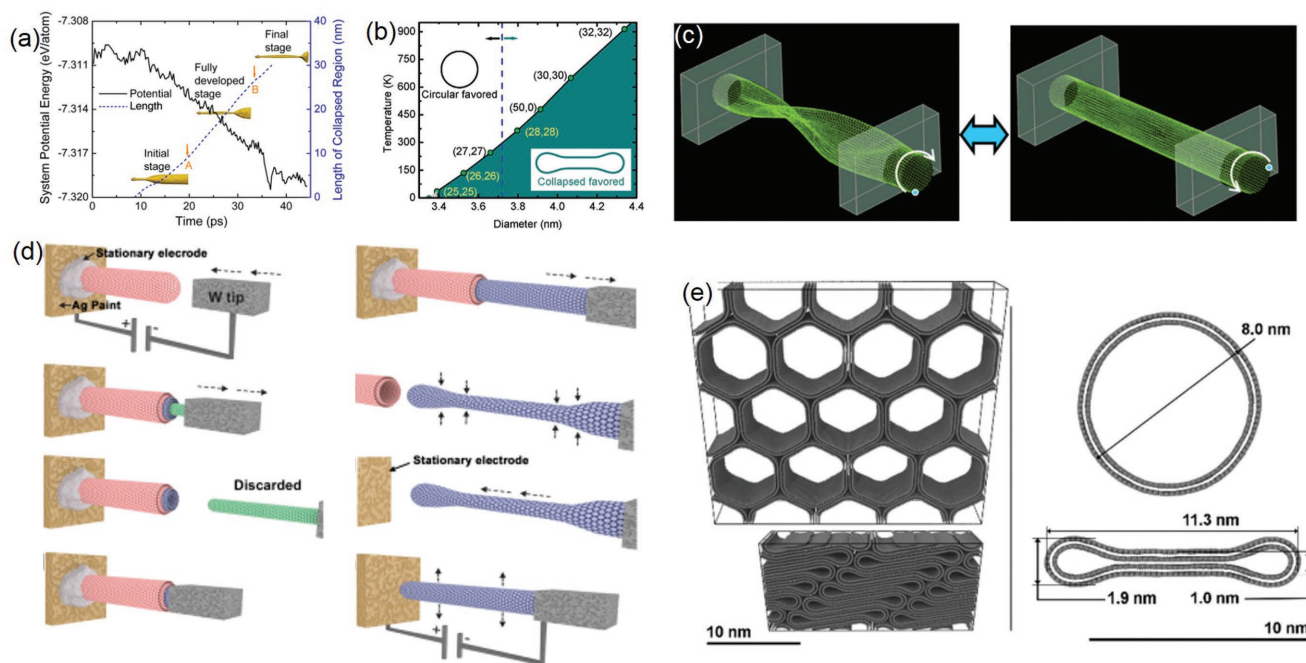


**Figure 6.** a)  $I$ – $V_G$  curve of a MWNT device (curve A) and a collapsed MWNT (curve B) of similar cross-section. Inset shows the configuration of the collapsed CNT. Reproduced with permission.<sup>[42]</sup> Copyright 1998, AIP Publishing. b) The system potential energy and the length of collapsed region versus time. Reproduced with permission.<sup>[43a]</sup> Copyright 2008, American Physical Society. c) Schematics of the proposed nanotorsional actuator, consisting of two states: collapsed and tubular. Reproduced with permission.<sup>[44a]</sup> Copyright 2012, Elsevier B.V. d) Schematic of method to produce and control CNT for reversible collapse and reinflation. Reproduced with permission.<sup>[45]</sup> Copyright 2016, American Chemical Society. e) Bulk CNT systems consisting of inflated CNTs and collapsed CNTs, demonstrating different densities. Reproduced with permission.<sup>[46]</sup> Copyright 2015, Elsevier B.V.

over the whole CNT at low temperature. When increasing temperature, the circular zone extends over the whole CNT with shrunk collapse zone. The reversible domino process is related to the different stable states of CNTs at different temperatures, which provides a route for energy conversion between thermal and mechanical energies. Consequently, a number of nanodevices, including heat engines, mechanical oscillators, nanoactuators, and rechargeable expelling devices, can be potentially fabricated.

By virtue of the state transition between tubular and collapsed CNT, Senga et al.<sup>[44]</sup> proposed a nanosized torsional actuator (Figure 6c). Both the ends of a collapsed and a twist CNT are connected to electrodes with one end free to rotate. When applying a sufficiently high current to the collapsed CNT, part of it change the collapse state to the tubular one. Once removing the current, the CNT reverts to the initial collapsed state. During the state change process, the free end rotates clockwise or counterclockwise. This nanoactuator would expand the fields related to functional nanomachines.

The geometrical transition between two forms of CNTs also inspires the fabrication of an inflatable nanoballoon actuator.<sup>[45]</sup> Figure 6d presents the schematic illustration of the electrostatically driven nanoballoon actuator. One end of CNT is first fixed to Cu grid with conductive paint, and the other end is then spot-welded to a tungsten tip. The move of tip to right extracts small-diameter core tubes, resulting in a daughter tube. Using the same welding and extracting process, it is possible to generate CNT susceptible to collapse. The collapsed CNT can be reinflated via applying an external voltage after contact with a stationary electrode. In situ TEM experiment employing a nanoelectromechanical manipulator realizes the prototype of an electrostatically driven nanoballoon actuator. The results have potential implications for general nanomatter manipulation.

Owing to their excellent mechanical properties, collapsed CNTs are the ideal structures for fabricating high-performance fibers or composites.<sup>[19a,46]</sup> Cylindrical CNTs cannot assemble into fibers or composites with a very high density (0.665 g cm<sup>-3</sup> for 8 nm CNTs). Together with the poor alignment of cylindrical CNT network, the relatively low packing density causes a high CNT–CNT interface thermal resistance, inhibiting sufficient thermal transport and causing a practical thermal conductance of only tens of W m<sup>-1</sup> K<sup>-1</sup>. By contrast, the collapsed 8 nm CNTs tend to form surface to surface stacking through shoulder to shoulder assemblies with a relatively high density (1.820 g cm<sup>-3</sup>). The high density and the low void volume fraction (Figure 6e) are essential for translating the mechanical properties to fibers and composites.<sup>[46]</sup> Consequently, the stacked architecture of long, collapsed CNTs could provide unidirectional thermal highways in lightweight functional composite material. Such CEGNRs thus would be applied as basic building blocks in high performance thermal materials.<sup>[31]</sup>

### 3. Preparation of CEGNRs

To harness the fascinating properties of CEGNRs and realize their potential applications, it is necessary to produce CEGNRs in controlled manners. Besides CVD and CNT coalescence, collapse of cylindrical CNTs or graphene tubes is the main

approach for preparing CEGNRs. In the following sections, strategies applied for generating CEGNRs will be addressed separately.

#### 3.1. CVD Synthesis of CEGNRs

Ribbon-like structures were first reported by Boehm through disproportionation of CO in 1973.<sup>[47]</sup> By optimizing the growth conditions, Murayama and Maeda<sup>[10a]</sup> prepared the ribbons in a high purity and investigated their structure in detail. Figure 7a presents a scanning electron microscopy (SEM) image of the carbon nanoribbon. High-resolution TEM image (Figure 7b) shows that the ribbon consists of carbon layers which are perpendicular to the ribbon axis. By analyzing the electron diffraction (ED) pattern of the catalyst particle, the particle structure is assigned as Fe<sub>3</sub>C. The interface between catalyst and ribbon is (103) Fe<sub>3</sub>C/(002) graphite, as schematically depicted in Figure 7c. It is noted that upon annealing at high temperature (2800 °C in Ar), the surface structure is converted into a frill-like structure, which can be considered as stacks of small CEGNRs.

Using the aerosol CVD process, production of crystalline GNRs was also reported by Campos-Delgado et al.<sup>[48,50]</sup> Figure 7d shows a typical SEM image of the as produced material, which consists of ribbons with width of 20–300 nm and thickness < 15 nm. The sharp edges of highly crystalline ribbons are either zigzag or armchair. Similarly, high temperature annealing could eventually lead to the defect-free samples, through graphitization and edge loop formation. Figure 7e,f, respectively, shows a SEM and a TEM image of ribbons after annealing at 2800 °C under Ar atmosphere for 30 min. Obviously, increasingly straighter lattice fingers, multiloop formation, and the annihilation of open edges are seen. Besides, the temperature effects of heat treatment are systematically studied, and the reconstruction of the ribbons at different temperatures is illustrated in Figure 7g. Similarly, Endo et al.<sup>[51]</sup> investigated the structural evolution of stacked cup carbon fibers upon heating above 1800 °C. Annealing at such a high reaction temperature stabilizes the edge sites with loop formation through folding of some planar hexagons. Starting from platelet carbon fibers, Lim et al.<sup>[49]</sup> performed different mechanical and chemical treatments, which induced the closed loop ends on the surface. By mechanical exfoliation, a primary structure unit of carbon fiber, which represents ultrashort CEGNR, is finally obtained (Figure 7h).

#### 3.2. Coalescence of CNTs

Different from the behaviors of carbon fibers, SWNTs could coalesce upon heating. Nikolaev et al.<sup>[52]</sup> first reported the coalescence-induced diameter doubling of SWNTs after heat treatment. Such a coalescence under electron beam irradiation and heating was later monitored by in situ TEM.<sup>[53]</sup> Building from these works, Kim et al.<sup>[54]</sup> modified the structure of bundled SWNTs by high-temperature heat treatment in vacuum. By carefully choosing the annealing temperature, two types of CEGNRs are formed from arc-discharge SWNTs. Figure 8a

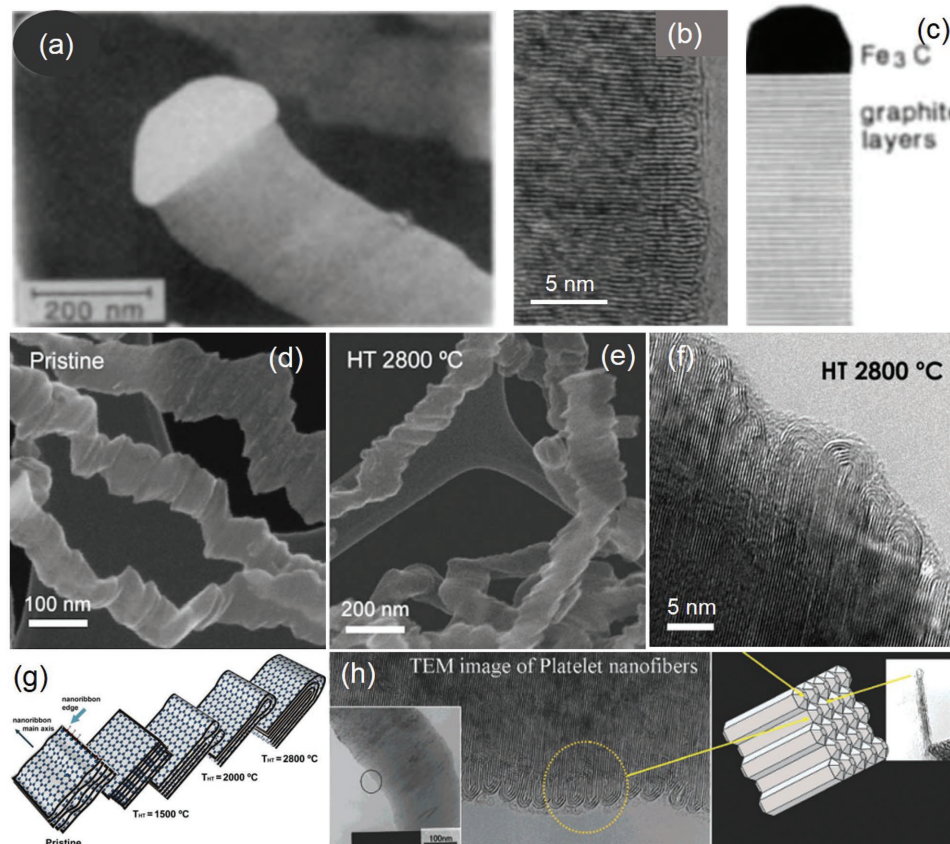


**Figure 7.** a) SEM image of ribbon-like structure synthesized at 700 °C. b) TEM image of the ribbon-like fiber with edges. c) Schematic illustration of the ribbon-like structure. d) SEM image of the as-produced ribbons. Reproduced with permission.<sup>[10a]</sup> Copyright 1990, Springer Nature. e) SEM image of the ribbons after heat treatment at 2800 °C for 30 min. f) TEM image of the ribbon after heat treatment. g) Schematic model for the restructuring process achieved by the thermal treatment. Reproduced with permission.<sup>[48]</sup> Copyright 2009, Elsevier B.V. h) TEM image of a platelet fiber, mechanically separated structural unit, and the suggested model. Reproduced with permission.<sup>[49]</sup> Copyright 2004, American Chemical Society.

shows a TEM image of product after annealing at 1800 °C. A stack of collapsed CNTs is clearly seen. The diameter of collapsed CNTs is much larger than the mean diameter (1.4 nm) of arc-discharge SWNTs, indicating the coalescence of SWNTs. Heat treatment at a higher temperature generates CEGNRs resembling collapsed MWNTs. Figure 8b,c depicts TEM images of the CEGNRs formed after heat treatment at 2200 °C. Schematic illustration for the generation of the two types of CEGNRs is presented in Figure 8d.

The CNT coalescence is supposed to follow a “patching-and-tearing” mechanism, as described by extensive MD simulations.<sup>[55]</sup> In the process, vacancies and dangling bonds are important to initialize the intertube polymerization, which is driven by strain energy minimization. In bundled SWNTs with less than 4 tubes, the “patching-and-tearing” process leads to the formation of large-diameter SWNTs or collapsed ones. During the thermal heating at temperatures higher than 1600 °C, vacancies are produced in the SWNTs and are highly mobile through the SWNTs. The vacancies keep migrating until they are trapped by dangling bonds in the adjacent tube, initializing the polymerization of SWNTs. The intertube links further evolve into “patches,” which are portions of an enveloping surface common to both the tubes (Figure 8e). The patches

develop in some portions of the SWNTs and some of them tear, resulting in partial coalescence (Figure 8e,  $t = 125$  ps). As the time evolves, the patches grow in the axial direction and merge with other newly formed or already existed patches. The two SWNTs eventually coalesce in the whole length (Figure 8e,  $t = 165$  ps). Depending on the diameter of the coalescent SWNT, the final configuration could be cylindrical SWNT or CEGNRs. In addition, for bundles with more than 4 tubes, the coalescence could lead to the formation of a cylindrical or a collapsed MWNT (Figure 8f).

### 3.3. Collapse of CNTs

In the CNT coalescence process, the CEGNRs are supposed to be directly formed by the “patching-and-tearing” mechanism.<sup>[55]</sup> However, there is a possibility that cylindrical CNTs first form from the SWNT coalescence and then collapse into the targeting GNRs, as the collapse of CNTs is energetically favored under certain conditions.<sup>[16a,17]</sup> In the past two decades, many experimental and theoretical works have been dedicated to determine the threshold diameters ( $R_{thr}$ ) and achieve collapsed CNTs.

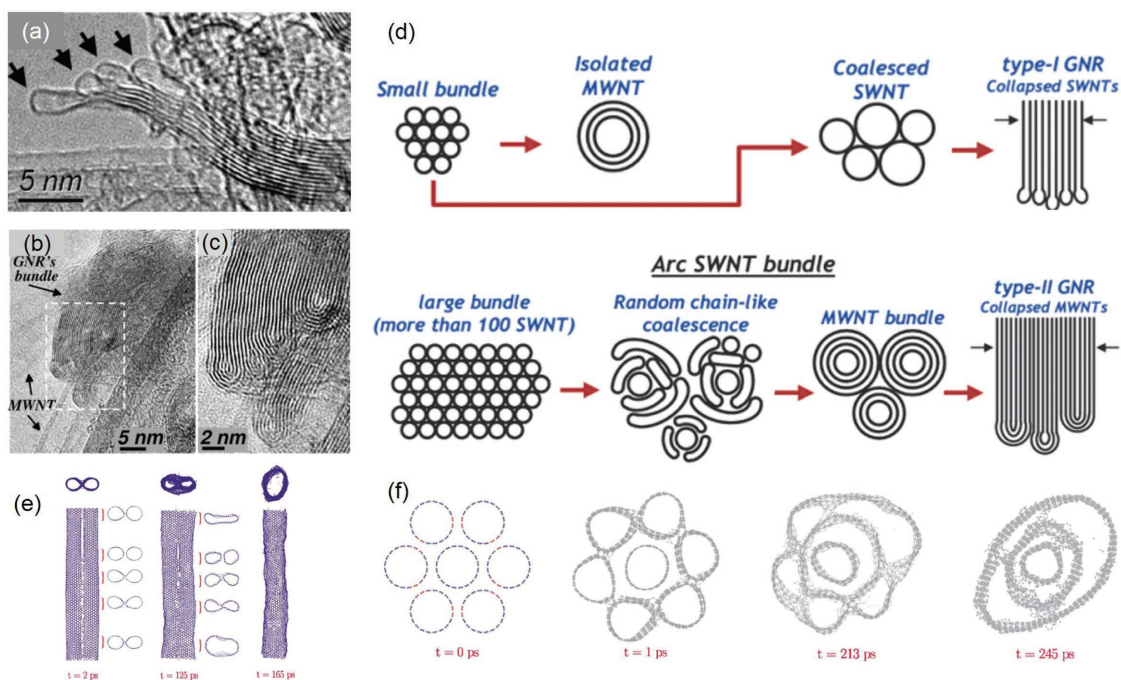


**Figure 8.** a) TEM image of arc-discharge SWNTs after heat treatment at 1800 °C. b,c) TEM image of arc-discharge SWNTs after heat treatment at 2200 °C. d) Schematic presentation of bundled arc-discharge SWNT evolution into different types of CEGNRs upon high temperature calcination. Reproduced with permission.<sup>[54]</sup> Copyright 2005, American Chemical Society. e) Snapshots taken from simulations showing the coalescence of two SWNTs. f) Snapshots showing the sequence of bundled SWNT to MWNT transformation. Reproduced with permission.<sup>[55]</sup> Copyright 2002, American Physical Society.

### 3.3.1. Threshold Diameter for Spontaneous Collapse of CNTs: Theoretical Predications

The energy characteristics of round and collapsed CNTs of various sizes are compared to estimate the threshold CNT diameters. The equilibrium cross-section of collapsed CNTs was first simulated by the continuum elasticity theory with a Lennard-Jones description of intersheet attraction.<sup>[17]</sup> In the elastic theory, the relevant parameter is  $\epsilon_{\text{attr}}/k$ , where  $\epsilon_{\text{attr}}$  represents interlayer attractions, and  $k$  is the graphite sheet mean curvature modulus. The  $\epsilon_{\text{attr}}/k$  determines the sizes of bulbs and the crossover between circular and collapsed configurations.

When performing calculations on  $R_{\text{thr}}$ , different approaches use different  $\epsilon_{\text{attr}}$ , which is reflected by a Lennard-Jones potential for carbon. Xiao et al.<sup>[23]</sup> adopted an  $\epsilon_{\text{attr}}$  of 2.39 meV when performing atomic scale finite-element method to determine the  $R_{\text{thr}}$  for SWNT collapse. For armchair SWNTs, the  $R_{\text{thr}}$  is 4.12 nm. By contrast, when applying an  $\epsilon_{\text{attr}}$  of 53.6 meV in MD simulations implemented in large-scale atomic/molecular massively parallel simulator (LAMMPS),  $R_{\text{thr}}$  is calculated to be 2.6 nm.<sup>[16b]</sup> However, the traditional Lennard-Jones potential has its intrinsic drawback that the vdW interaction between graphene layers are almost independent of the stacking pattern. For example, the vdW energy difference between AA and AB stacking graphene is only 0.5%. Using atomistic simulation, Liu et al.<sup>[56]</sup> studied the effect of interlayer lattice registry on the formation of fully collapsed SWNTs. In the work, various types of SWNTs with different chiralities but approximately the same diameters are modeled. After SWNT collapse, the alignment angles  $\alpha$  between the opposite graphene layer are

in the range of 0°–60°. **Figure 9a** presents the system energy as a function of alignment angles. Collapsed (80, 0) SWNT with  $\alpha = 0^\circ$  exhibits the largest energy per atom (−0.03613 eV), corresponding to the smallest vdW interaction. By contrast, collapsed (40, 40) SWNT with  $\alpha = 60^\circ$  demonstrates the smallest energy per atom (−0.03692 eV) and the largest vdW interaction. For collapsed chiral SWNTs, the energy per atom shows weak dependence on the alignment angle, although there are some local minimums in the energy state (−0.03667 eV). This work shows a relatively large difference in lattice registry-sensitive vdW interactions.

To estimate the error and precisely determine the vdW interaction between the graphene layers, Ding and co-workers<sup>[16d]</sup> performed Grimme's density functional theory-D2 (DFT-D2) calculations. **Figure 9b** shows the vdW attractive energy of bilayer graphene with different stacking patterns. The vdW interaction between a rotated bilayer graphene is about 10.75% lower than that of the AB stacked one. Therefore, a 10.75% decrease in the effective vdW interaction should be considered unless the collapsed SWNTs have the AB stacking configuration. Besides the stacking order, the thermal fluctuation in collapsed SWNTs could also affect the vdW interaction between the opposite graphene sheets. As calculated by the MD simulation, the vdW energy of collapsed SWNTs is a function of temperature (**Figure 9c**). Compared with the bilayer graphene, which shows a 1.92% of reduction in the vdW interaction if the temperature is increased from 0 to 300 K, the vdW interactions within a collapsed (30, 15) SWNT is reduced by 4.38%.

Overall, whether a SWNT spontaneously collapses or not mainly depends on energy competition between the curvature

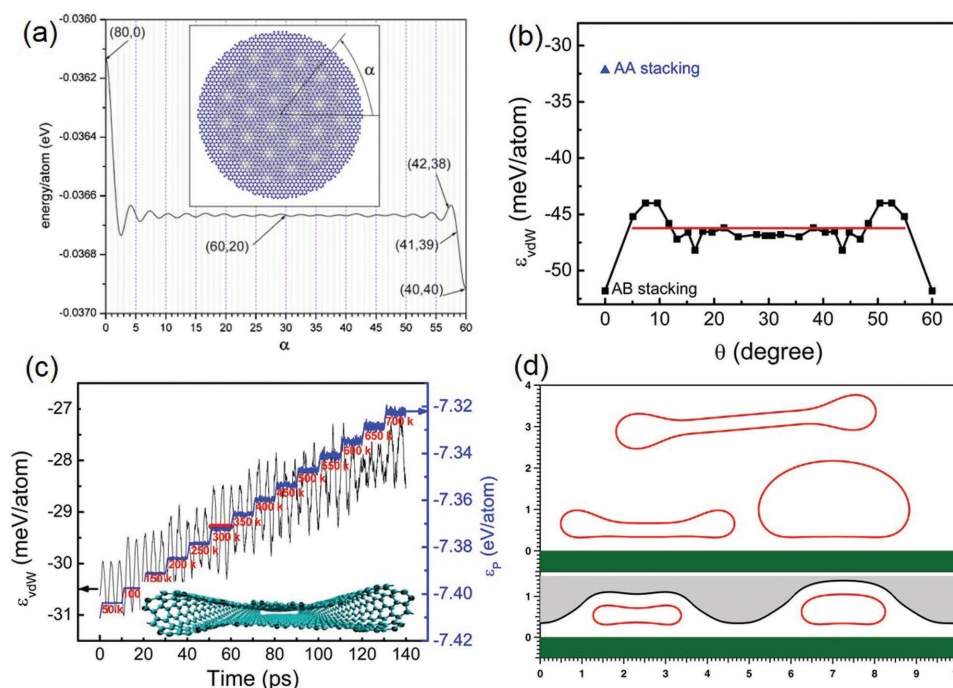


**Figure 9.** a) The system energy as a function of alignment angle for two parallel graphenes. Reproduced with permission.<sup>[56]</sup> Copyright 2004, American Physical Society. b) The vdW attractive energy of bilayer graphene with different stacking patterns. c) The vdW energy and total potential energy as a function of MD simulation time and temperature. Reproduced with permission.<sup>[16d]</sup> Copyright 2014, American Chemical Society. d) SWNT geometries for diameters near  $R_{thr}$ : 4.3 nm for freestanding one, 2.9 nm for SWNT on a substrate, and 1.6 nm for SWNT under metal. Reproduced with permission.<sup>[25a]</sup> Copyright 2014, American Chemical Society.

energy and the vdW interaction, which is coherently related to SWNT diameter. However, the energies differ from each other when performing calculations using different methods and different parameters, accounting for the discrepancy in  $R_{thr}$ . **Table 1** summarizes the  $R_{thr}$  for SWNT calculated from different groups using different methodologies. Clearly, the adopted  $\epsilon_{vdW}$  shows striking differences and the calculated  $R_{thr}$  ranges from 1.0 to 7.0 nm. Besides, whether the SWNT is suspended or lying on a substrate could greatly influence the value of  $R_{thr}$ . For example, using MD simulations, Yan et al.<sup>[57]</sup> investigated the radial collapse of SWNTs on  $Cu_2O$  substrate. The vdW force between SWNT and  $Cu_2O$  substrate promotes the collapse. As a result, the system could be stable even though the collapse costs large deformation energy. Therefore,  $R_{thr}$  is determined to be 1.0 nm, where the full collapse occurs. It is noted that the surface energy of the support, which governs the vdW interactions between SWNT and substrate, also plays an important role in determining the  $R_{thr}$ . Perebeinos and Tersoff<sup>[25a]</sup> investigated the SWNT deformation and collapse under Pd contacts having a surface energy of  $12.5 \text{ eV nm}^{-2}$ . The  $R_{thr}$  of a freestanding SWNT is calculated to be 4.3 nm, the structure of which is presented in Figure 9d. When lying on a graphene substrate, the vdW bonding to the substrate is increased with the collapsed geometry, reducing the  $R_{thr}$  to 2.9 nm. The deformations become even stronger under a metal Pd because of the presence of the capillary “pressure.” The SWNT collapse and flattening lower the energy by reducing the metal surface area at the cost of SWNT bending energy. Consequently, a much smaller  $R_{thr}$ , 1.6 nm, is obtained on the graphene substrate.

Similarly, SWNTs in bundles could have a smaller  $R_{thr}$  because of the presence of vdW interactions among the SWNTs.<sup>[58]</sup>

With the increase of wall number ( $N$ ),  $R_{thr}(N)$  increases.<sup>[16b,17,23]</sup> This is because the attractive energy after collapse is roughly independent of the number of tube wall, while the curvature energy gain increases with increased wall number. For example, the  $R_{thr}(6)$  for a six-wall CNT is calculated to be 8.6 nm at an  $\epsilon_{attr}$  of 0.025 eV per atom.<sup>[17]</sup> With increase of wall number, an increase in the  $R_{thr}$  of the innermost wall is required to govern the stable, and fully collapsed CNTs.

### 3.3.2. Threshold CNT Diameter for Spontaneous Collapse: Experimental Evidences

Despite the great efforts in calculating the  $R_{thr}$  for the spontaneous collapse of SWNTs, plausible experimental evidence in determining the  $R_{thr}$  value has been scarce.<sup>[16b,d,19a]</sup> This is mainly due to the difficulties in achieving collapsed SWNTs in a reasonable quantity. Although SWNTs with diameters larger than 2 nm are readily produced, collapse of CNTs is rarely claimed. For example, Cheung et al.<sup>[67]</sup> synthesized large-diameter CNTs from monodisperse Fe nanoparticles. Using 9 nm Fe particles, SWNTs and double-walled CNTs with an average diameter of 7 nm were yielded. However, no collapse of the CNTs was reported. Using tailored trilayered Fe/ $Al_2O_3/SiO_2$  as the catalyst, Han and Ostrikov<sup>[68]</sup> synthesized vertically aligned SWNTs with a mean diameter larger than 5 nm. Even though the SWNTs aggregate into small bundles,

**Table 1.** Summary of  $R_{\text{thr}}$  values of SWNTs in the literature and the employed methodologies. The values of vdW interaction between graphene layers are indicated.

$R_{\text{thr}}$ [nm]	Methodology	$\epsilon_{\text{vdW}}$	Ref.
2.6	Simple model analysis using a DFT-based curvature energy and a vdW interaction	20 eV Å <sup>-2</sup>	[16a]
1.8–4.4	Continuum model analysis	25–100 meV per atom	[17]
3.0	Molecular dynamics simulation	31.8–32.3 meV per atom	[59]
3.4	Molecular dynamics simulation	35 ± 15 meV per atom	[60]
2.0	Molecular dynamics simulation	2.84 meV <sup>a)</sup>	[61]
4.1	Atomistic simulation	36.1–36.9 meV per atom	[23,56]
4.2–6.9	NσT ensemble molecular dynamics simulation	4.1 meV <sup>a)</sup>	[58a]
0.98	Continuum model analysis and molecular simulation	2.50 eV nm <sup>-2</sup>	[21]
6.2	Atomistic molecular mechanics	2.39 meV per atom	[62]
7.0	Continuum analysis using a DFT-based elasticity model	55 meV per atom	[63]
1.0	Molecular dynamics simulation	2.67 eV nm <sup>-2</sup>	[57]
1.9	Atomistic simulations and continuum analysis	2.39 meV per atom	[64]
2.6	Molecular dynamics simulation using LAMMPS	53.6 meV per pair	[16b]
2.27	Continuum elasticity model analysis	2.78 meV per atom	[65]
2.02	Continuum mechanics analysis and molecular mechanics simulations	2.84 meV per atom	[26]
1.63	Molecular dynamics simulation	2.67 eV nm <sup>-2</sup>	[24]
4.3 (2.9)	Full calculation	60 meV per atom	[25a]
5.1	Molecular dynamics simulation	2.84 meV per atom	[16d]
5.1	DFT calculations with DFT-D2	52 meV per atom	[66]

<sup>a)</sup>Depth of Lennard-Jones potential well.

whether the large diameter SWNTs are collapsed or not is overlooked.

The negligence of CNT collapse in the previous works is mainly due to the difficulties in discriminating collapsed CNT from cylindrical one. High-resolution TEM has been widely applied to characterize collapsed CNTs.<sup>[16a,19a]</sup> Although collapsed CNTs have distinct signatures, a sample rotation study is generally necessary to unambiguously confirm the flattened feature of a collapsed CNT.<sup>[16a]</sup> Zhang et al.<sup>[16b]</sup> adopted deformed structures, including kinked, folded, and twisted structures, as the identifier of CEGNRs. However, the local deformation is not necessarily initiate the full collapse of a SWNT.<sup>[69]</sup> Indeed, the  $R_{\text{thr}}$  determined in the work is relatively small (2.6 nm for SWNT and 4.0 nm for double-walled CNTs), questioning the reliability of the CNT collapse identification technique.

To unambiguously distinguish the collapsed CNTs from inflated ones, nanobeam ED is proposed.<sup>[16d]</sup> In the ED pattern of a SWNT, a strong equatorial oscillation and nonequatorial layer lines, which are associated with SWNT chirality and described by Bessel functions with certain orders, are clearly seen (Figure 10a). The spots are elongated, and their intensities fade away toward the exterior, arising from the curvature and the finite lateral size of SWNTs. By contrast, the ED pattern of a collapsed SWNT (Figure 10b) differs greatly from that of an inflated one. Remarkably, the equatorial line vanishes, and the geometry of diffraction spots resembles that of bilayer graphene. Using the nanobeam ED strategy, He et al.<sup>[70]</sup> systematically investigated isolated SWNTs grown on a porous Si<sub>3</sub>N<sub>4</sub> grid. When using CH<sub>4</sub> as the carbon source, the synthesized SWNTs

tend to adopt a tangential mode,<sup>[22b]</sup> leading to the synthesis of SWNTs with diameters correlated with the catalyst particles. All the obtained SWNTs in the diameter range of 1.0–4.7 nm maintain their inflated geometry. This work suggests that the  $R_{\text{thr}}$  for individual, freestanding SWNTs should be larger than 4.7 nm.

Using TEM image, Motta et al.<sup>[19a]</sup> observed collapsed CNTs withdrawn directly from gas phase CVD. Figure 3g shows a typical TEM image of a fractured bundle CNTs with the “dog bone” cross-section. Altogether, five SWNTs with diameters in the range of 4.59–5.66 nm were observed and all of them are collapsed. This work indicates that the  $R_{\text{thr}}$  for bundled SWNTs is close to 4.6 nm. Different from SWNTs, double-walled CNTs are the major components and are frequently observed in the fiber. Based on extensive examination, it is revealed that most double-walled CNTs with diameters larger than 6.0 nm are collapsed, while small diameter ones (smaller than 5.0 nm) preserve their cylindrical configurations. The observation suggests that the  $R_{\text{thr}}(2)$  could be close to 6.0 nm.

The effect of bundling promotes the CNT collapse, thus complicating the determination of the  $R_{\text{thr}}$  for CNTs. On the basis of ED characterizations on a number of large diameter SWNTs grown from Au nanoparticles,<sup>[16d]</sup> some solid conclusions are made. On one hand, SWNTs with local deformation like kinks still preserve their cylindrical configuration (Figure 10c), excluding the validation of using such character to identify the collapsed geometry.<sup>[16b]</sup> On the other hand, the  $R_{\text{thr}}$  for SWNT collapse is determined to be 5.1 nm (Figure 10d), which is consistent with the calculation when choosing appropriate parameters and taking the thermal effect and stacking

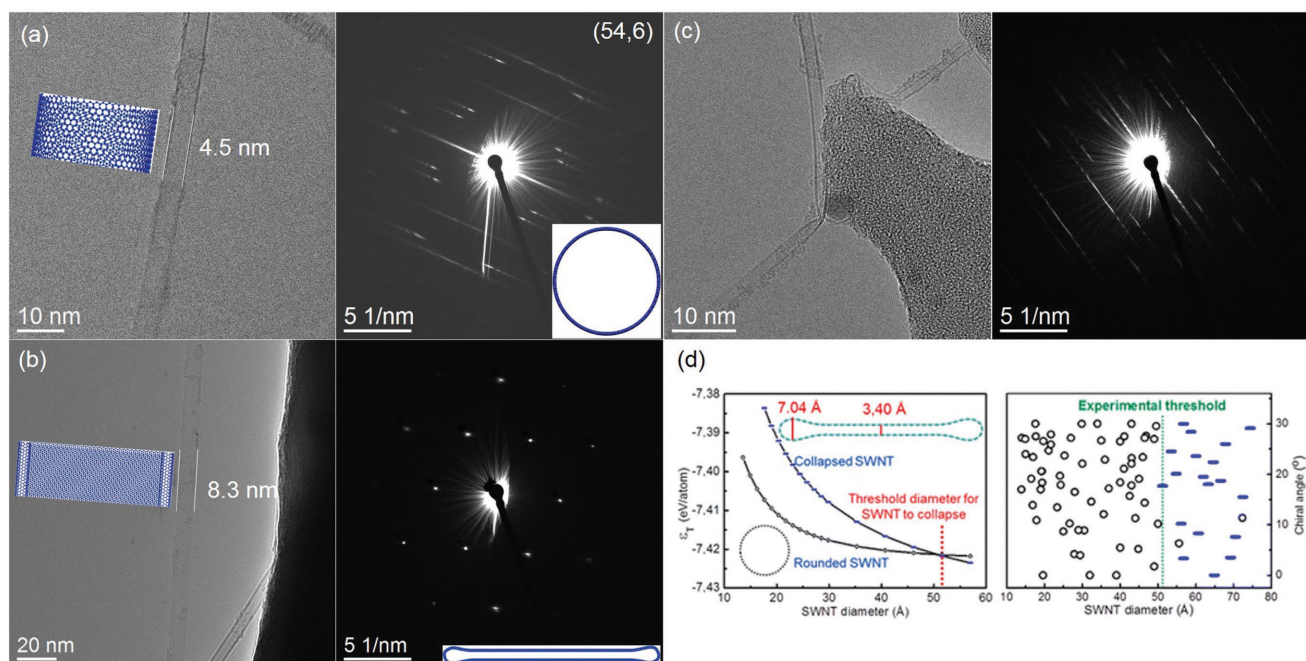


**Figure 10.** a) TEM image of an individual, cylindrical SWNT and its ED pattern. b) TEM image of a collapsed SWNT and its ED pattern. c) TEM image of a SWNT with kink and the ED pattern taken from a straight section. d) The determined  $R_{thr}$  for SWNT from simulations (left) and nanobeam ED experiment (right). Reproduced with permission.<sup>[16d]</sup> Copyright 2014, American Chemical Society.

effect into account. However, owing to the limited experimental results on collapsed CNTs with large wall numbers, the  $R_{thr}(N)$  for CNTs other than SWNTs remains controversial.

### 3.3.3. Synthesis of CEGNRs from CNT Collapse

**Templated Synthesis of CEGNRs:** Despite of the controversy in the exact value of  $R_{thr}$  for CNTs with different wall numbers, it is widely accepted that a large inner diameter facilitates the collapse of CNTs or graphene tubes. Templated synthesis of CNTs provides a facile approach for achieving structures with large inner diameters. Using porous anodic alumina as a template, Lin et al. synthesized CEGNRs with controlled sizes by CVD.<sup>[71]</sup> **Figure 11a** illustrates the experimental procedure and **Figure 11b** shows a TEM image of the as-prepared carbon nanostructure. Inset presents a high-resolution image, showing that the wall thickness is about 6.3 nm. The inner diameters of the CNTs are estimated to be 300 nm, and their collapse state is energetically favorable. Indeed, the final materials exhibit a width of  $470 \pm 80$  nm, which is larger than the diameter of the template channel, suggesting the collapse of produced structures after template removal. The crystallinity of collapsed CNTs could be greatly enhanced by annealing at high temperatures. **Figure 11c** presents the TEM image of an 800 °C-annealed GNR and its diffraction pattern (inset). Such a pair of prominent (002) diffraction spots suggests the good crystallinity of the GNRs while preserving their isolate configurations.<sup>[71]</sup> This approach provides a facile means to achieve CEGNRs with relatively large widths.

Besides porous alumina channels, other nanomaterials, such as metal-containing nanowires,<sup>[37,72]</sup> could serve as a sacrificial

template for the synthesis of GNRs. For example, Yu et al.<sup>[37]</sup> reported the synthesis of CEGNRs using Pd nanowire template. In their approach, Si-/SiO<sub>2</sub>-supported Pd nanowires are first placed into a plasma enhanced CVD chamber on which the graphene layers are grown. After Pd etching using diluted HNO<sub>3</sub>, graphene layers would collapse into CEGNRs if the layers are thin enough. On the contrary, the graphene tubes might retain their tubular structure if the graphene layers are sufficiently thick (**Figure 11d**). As a result, the final configuration of the product can be controlled by tuning the number of graphene layers deposited on Pd nanowires. **Figure 11e** shows a Pd nanowire (dark area) uniformly coated with graphene layers (white on the surface) after CVD. After the removal of Pd wires, hollow graphene layers are left exclusively. **Figure 11f,g** shows graphene layers with different thicknesses achieved by tuning the amount of C<sub>2</sub>H<sub>4</sub> during growth process. For thick graphene layers, their tubular structure could be maintained after Pd wire removal (**Figure 11f**). By contrast, thin graphene layers tend to collapse into graphene tubes, i.e., CEGNRs (**Figure 11g**). Similarly, scalable synthesis of few layer GNRs with controlled morphologies was also achieved by ZnS-templated CVD process.<sup>[72]</sup> However, due to the lack of detailed characterizations on the edge structures, it is unclear whether the edges of obtained GNRs are closed or open.

**Template-Free Synthesis of Collapsed CNTs:** Different from the abovementioned template technique, where the template must be removed after CVD growth, direct growth of CNTs favorable for collapse could be achieved. Employing a Fe<sub>2</sub>O<sub>3</sub>/Al<sub>2</sub>O<sub>3</sub> catalyst, Zhang and Jia<sup>[73]</sup> efficiently synthesized fully collapsed CNTs through catalytic decomposition of CH<sub>4</sub>. **Figure 12a** shows the SEM image of the curved belt-like structures with tens of micrometers long. TEM characterizations (**Figure 12b**)

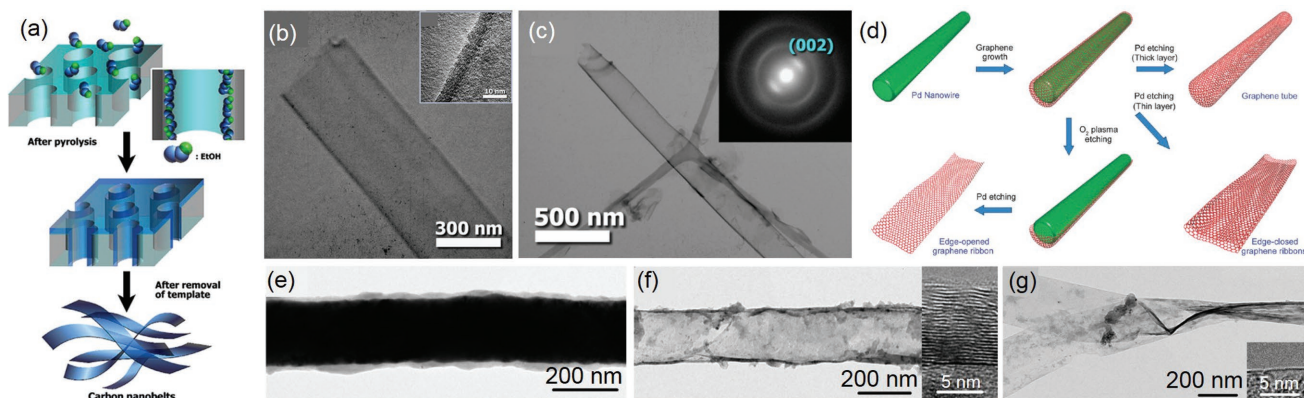


**Figure 11.** a) Schematic illustration of CEGNR formation using porous alumina as the template. b) TEM image of the as-obtained GNR. Inset shows the high-resolution image of the edge. c) TEM image of the CEGNR after heat treatment at 800 °C. Inset shows the diffraction pattern of the ribbon. Reproduced with permission.<sup>[71]</sup> Copyright 2008, Elsevier B.V. d) Schematic of the process for CEGNR fabrication using Pd nanowires as the template. e) TEM image of graphene layers on Pd nanowire. f) TEM image of graphene layers (23 layers) after Pd removal. g) TEM image of single graphene layer after removing Pd wire. Insets are high-resolution image of the graphene layers. Reproduced with permission.<sup>[37]</sup> Copyright 2010, American Chemical Society.

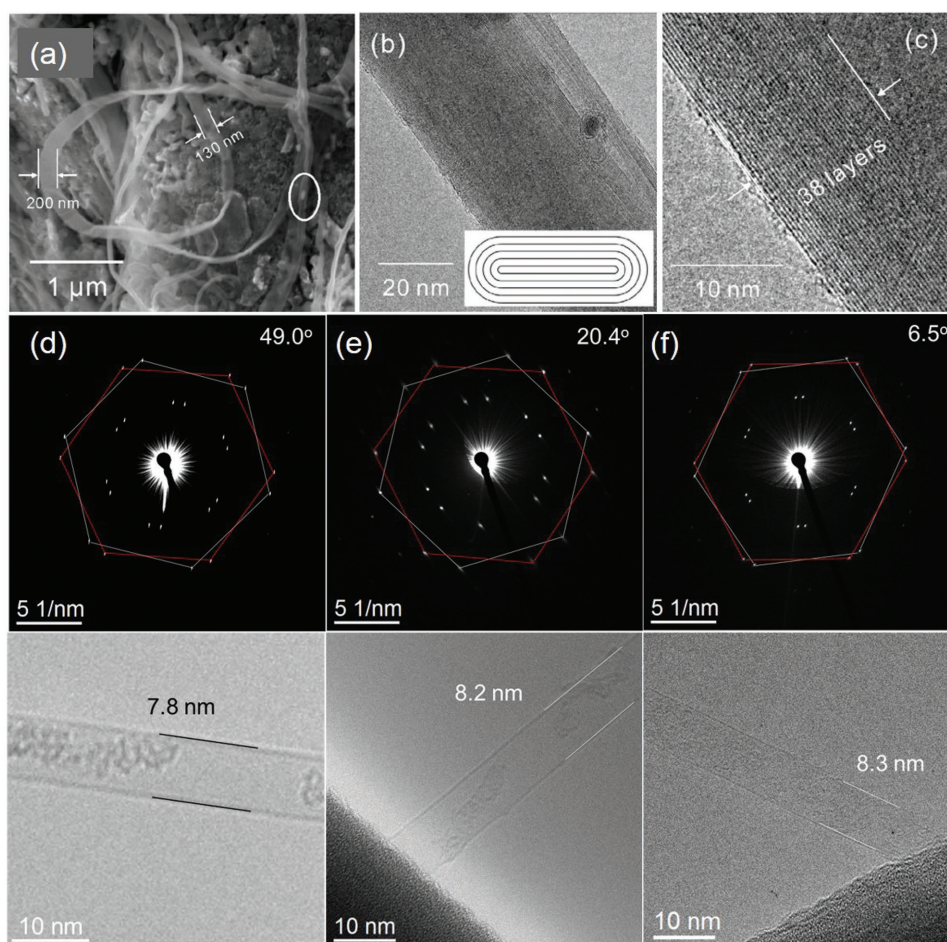


**Figure 12.** a) SEM image and b, c) TEM images of collapsed CNTs grown on  $\text{Fe}_2\text{O}_3/\text{Al}_2\text{O}_3$  catalyst. Reproduced with permission.<sup>[73]</sup> Copyright 2015, Elsevier B.V. d–f) ED patterns of three CEGNRs from collapse of SWNTs and their corresponding TEM images. Reproduced with permission.<sup>[16d]</sup> Copyright 2014, American Chemical Society.

confirm that the product is a single collapsed CNT, as schematically illustrated in the inset. The interlayer spacing is 0.353 nm, larger than that of CNTs, suggesting the presence of the repulsive force between the graphite layers. This work opens a new and simple way for synthesizing fully collapsed CNTs. However, owing to the relatively large size of the catalytic Fe particles, the collapsed CNTs usually have a relatively large number of walls. For example, the CNT presented in Figure 12c possesses 38 graphite layers.

Compared to MWNTs, SWNTs have a smaller  $R_{thr}$  to collapse. However, simply increasing the catalyst particle does not necessarily lead to the formation of SWNTs with large diameters. Owing to the high carbon solubility in catalyst like Fe, large size particles could cause the growth of MWNTs. To circumvent the synthesis of MWNTs on large catalyst particles, Au nanoparticles, which are known to possess a low carbon solubility, are adopted to grow large diameter SWNTs.<sup>[16d]</sup> In the experiment, 10 nm Au nanoparticles are first dispersed onto  $\text{Si}_3\text{N}_4$  grid and annealed in air to activate the catalyst.<sup>[74]</sup> CVD growth of SWNTs is carried out at 900 °C using  $\text{CH}_4$  as the carbon source. Figure 10a presents a TEM image of a SWNT and its corresponding nanobeam ED pattern, respectively. The ED pattern displays a strong equatorial oscillation and layer lines, the spots of which are elongated, characteristics of a cylindrical SWNT arising from the tube curvature and the finite lateral size. The chirality of the SWNT is assigned as (54, 6), a metallic SWNT with diameter of 4.5 nm. Besides large diameter SWNTs with inflated configuration, collapsed SWNTs are also observed in the Au-grown product. Figure 10b shows the TEM image of a collapse SWNT, the width of which is 8.3 nm. The collapse state of the SWNT is confirmed by its ED pattern, which demonstrates hexagonal patterns with spacings and symmetry consistent with those of graphene. The stacking orders of the collapsed SWNTs inherit the chiral angles of

their inflated counterparts. As a result, CEGNRs with different stacking orders can be achieved from the collapse of SWNT (Figure 12d–f). This work would guide the design of catalyst particles for growing large diameter SWNTs which tend to collapse spontaneously.

**Extracting Shells from MWNTs:** CNTs with larger inner diameters can also be achieved by extracting shells from MWNTs. By employing current-induced electrical breakdown, Kim et al.<sup>[75]</sup> reported the production of GNRs from MWNTs in a high vacuum, nonchemical environment. In the experiment, a movable electrode, which is attached with a MWNT, is sliding to generate GNRs with the assistance of proper voltage bias control. The applied electric current has two roles: one is to break C–C bond along the current direction; the other is to weld and fix the CNT. Under suitable electrical current, the GNR could be formed by sliding the GNR and the inner core of the MWNT. Unfortunately, the atomic resolution characterizations on the edge structures are lacking.

CEGNRs are unambiguously obtained by telescopically extracting shells from MWNTs using a nanomanipulator inside TEM.<sup>[16c]</sup> The schematic illustration of the process and experimental results are, respectively, presented in Figure 13a,b. Initially, one end of conventional MWNT is fixed via silver paint to a TEM grid, which is subsequently attached to a stationary sample holder. Subsequently, the other end of the tube is spot-welded by applying a bias voltage. As the tungsten tip moves away, it extracts the outer layers of the parent tube, yielding CNTs with few walls and relatively large diameters. When a long enough daughter CNT is generated, its collapse can be easily initiated by a small displacement of the tungsten tip transverse to the tube axis. The maximum length of the collapsed CNT is equal to the length of the parent CNT. This work demonstrates the use of nanomanipulator to create CEGNRs by telescoping them from the fixed core.

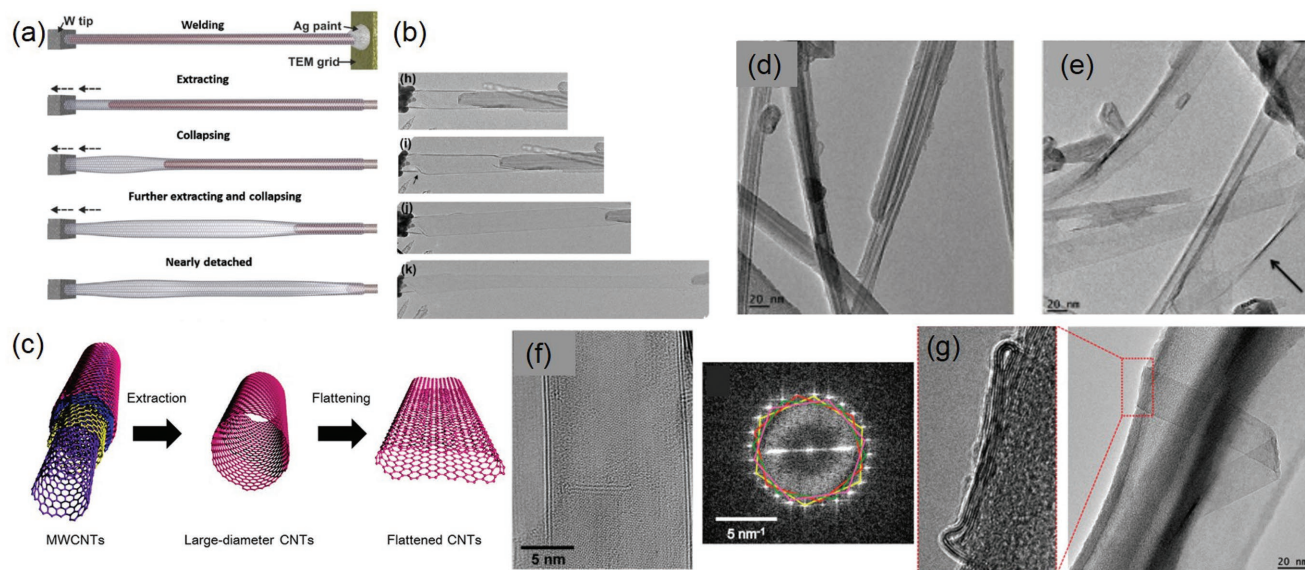


**Figure 13.** a) Schematic of experimental setup and b) the corresponding TEM images for generating CEGNRs by extracting shells from MWNTs. c) Schematic representation of the solution procedure for preparing CEGNRs. Reproduced with permission.<sup>[16c]</sup> Copyright 2016, Tsinghua University Press and Springer-Verlag Berlin. d) TEM image of raw MWNTs. e) TEM image of obtained CEGNRs. f) High-resolution TEM image of an isolated CEGNR and its fast Fourier transformation pattern. g) TEM image of the cross-section of a GNR. Reproduced with permission.<sup>[76]</sup> Copyright 2013, Springer Nature.

Although the use of nanomanipulator in TEM allows in situ track of the extraction and the collapse of CNTs, the process is costly and not applicable for large-scale production. A high yield production of fully collapsed CNTs was reported by Choi et al.,<sup>[76]</sup> who developed a solution-based approach to extract the inner tubes from larger-diameter MWNTs (Figure 13c). After the inner tube extraction, the large diameter CNTs spontaneously collapse to form flatten GNRs. The starting materials are commercial MWNTs (Figure 13d), which have a diameter of 13 nm and the average wall number is 5. Prior to the extraction, the caps of MWNTs are opened by air oxidation. The opened CNTs are subsequently sonicated in surfactant solution or dichloroethane for 1 h. Figure 13e shows TEM image of the sample after sonication. The typical diameter of the sample increases to 20 nm and the wall number decreases to 2–3. Fast Fourier transformation image demonstrates four sets of hexagonal patterns, consistent with that of bilayer graphene nanoribbons (Figure 13f). The cross-section of the material is further characterized to confirm the collapsed structure (Figure 13g). This work provides a facile method for large-scale production of close-edged GNRs, which has great potential for future electronics and basic research.

### 3.3.4. Collapse of CNTs by External Forces

Besides the spontaneous collapse of CNTs with relatively large inner diameters, other strategies, such as applying external mechanical forces, exerting hydrostatic pressure, irradiation using TEM electron beam, ball milling, and electrical unwrapping, would induce the collapse of CNTs. Yakobson et al.<sup>[77]</sup> simulated the transformation of CNTs subjected to large

deformation using a realistic many-body potential. The simulations show that under mechanical duress, a deformation which is proportional to the external force initially occurs. Further increasing the external force eventually leads to the collapse of CNTs. In the following subsections, different forces adopted to induce the collapse of CNTs are separately addressed.

**Hydrostatic Pressure-Induced CNT Collapse:** An exceptionally large and reversible volume reduction of SWNTs was observed when compressing them.<sup>[78]</sup> In the experimental work, the starting materials are purified, highly crystalline SWNTs. A piston-cylinder apparatus was applied to determine the volume change as a function of pressure. After several cycles, all the behaviors are reproducible. Figure 14a shows the deduced SWNT density as a function of applied pressure. The starting density of the compressed SWNTs is  $\approx 1.5 \text{ g cm}^{-3}$ , which is close to the crystallographic density ( $1.33 \text{ g cm}^{-3}$ ), suggesting that all the porosity has been compacted out. The calculated compressibility for fully compacted SWNTs at 1 atm is about  $100 \times 10^{-3} \text{ kPa}^{-1}$  and decreases to  $(6\text{--}10) \times 10^{-3} \text{ kPa}^{-1}$  at high pressure, which is still a factor of 3–5 greater than the theoretical value. Such a high compressibility and the large volume reduction indicate the existence of volume-reducing deformation of SWNTs, i.e., the cylindrical SWNTs are crushed into elliptical cross-section. After the release of the pressure, the elliptical cross-section of SWNTs are back to cylindrical one, suggesting that the compression process is reversible. Tang et al.<sup>[79]</sup> measured the volume compressibility of SWNTs by in situ synchrotron X-ray diffraction (Figure 14b), showing that the characteristic SWNT lattice deflection is diminished beyond 1.5 GPa. The lattice disappearance could arise from a structure deformation, which is reversible up to 4 GPa. That is, the diminished SWNT reflection reappears when the pressure is

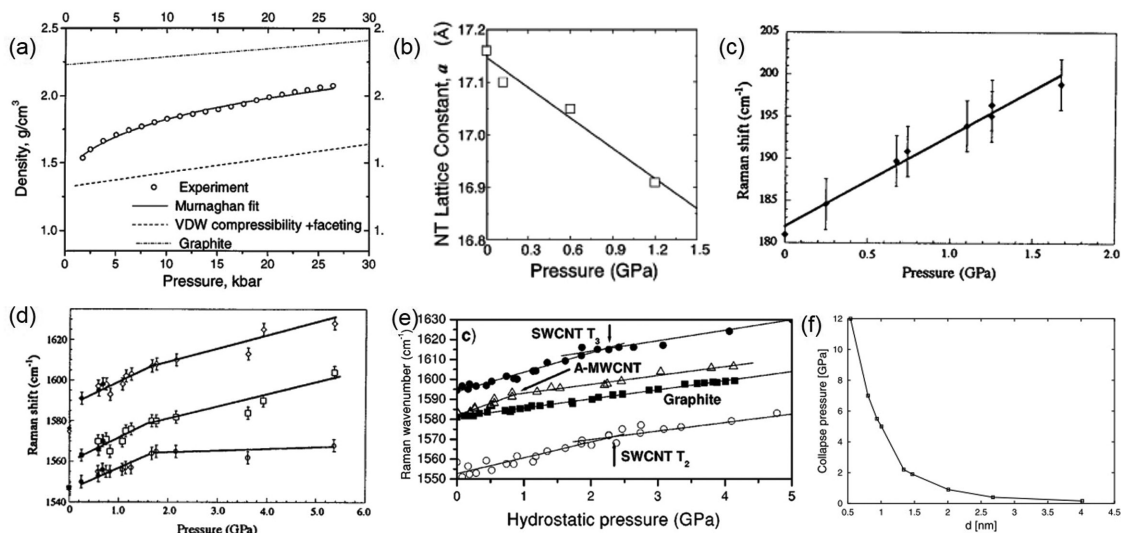


**Figure 14.** a) The density versus pressure in compacted SWNT sample. Reproduced with permission.<sup>[78]</sup> Copyright 1999, American Physical Society. b) Lattice constant of CNT as a function of pressure measured by in situ synchrotron X-ray diffraction. Reproduced with permission.<sup>[79]</sup> Copyright 2000, American Physical Society. c) Raman shift in the RBM mode of SWNTs as a function of pressure. Reproduced with permission.<sup>[80]</sup> Copyright 2000, American Physical Society. d) Raman shift versus pressure for the G mode of SWNTs. Reproduced with permission.<sup>[81]</sup> Copyright 1999, American Physical Society. e) Comparative plot of the Raman high-frequency peak positions for SWNTs, MWNTs, and graphite. Reproduced with permission.<sup>[82]</sup> Copyright 2003, American Physical Society. f) Collapse pressure of SWNT bundles along loading branch as a function of tube diameter. Reproduced with permission.<sup>[58a]</sup> Copyright 2004, American Physical Society.

released. However, beyond 5 GPa, the SWNT reflection could not recover, which is caused by the destroy of SWNT lattice structure, i.e., SWNTs are fully collapsed.

The phase transition in SWNT structure is also reflected by the Raman shift as functions of pressure. Peters et al.<sup>[80]</sup> monitored the radial breathing mode (RBM) and tangential mode evolution of SWNTs at high pressures. The RBM shifts to higher frequency with a slope of  $10.1 \pm 1.2 \text{ cm}^{-1} \text{ GPa}^{-1}$  (Figure 14c). At pressures above 1.7 GPa, the vanishing of RBM indicates a dramatic change in SWNT structure. Similarly, the high energy graphite (G) mode demonstrates a response at high pressure different from that at low pressure (Figure 14d). At low pressure, the slopes for all the three peaks are all consistent with the calculation results.<sup>[81]</sup> At pressures above 1.7 GPa, the rates of frequency change for all the peaks decrease abruptly, suggesting the deformation of the SWNT cross-section.

Sandler et al. compared the pressure-induced Raman peak shifts of various carbon nanostructures.<sup>[82]</sup> All hollow CNTs display two distinct regimes with a transition pressure that varies for different materials (Figure 14e). At low pressure range, steeper slopes are observed for all CNT samples. The slopes become shallower and lie approximately parallel to the graphite line at higher pressures. The high-pressure results are interpreted as the complete collapse of CNTs resembling graphite. Subsequently, Elliott et al.<sup>[58a]</sup> performed a series of MD simulations to test the hypothesis and investigated the pressure dependences of SWNT collapse. Clearly, the SWNT collapse pressure mainly depends on the tube diameter (Figure 14f). These works provide a way for CNT collapse by applying large enough hydrostatic pressures.

**Electron Beam Irradiation–Induced CNT Collapse:** Using high energy electron irradiation in high-resolution TEM, MWNT collapse was in situ studied.<sup>[83]</sup> In the experiment, the accelerating voltage for CNT collapse investigation is 800 keV. The initial inner CNT diameter of 1.6 nm decreases dramatically to 1.2–0.8 nm at 60 s. Meanwhile, the lattice fringes are no longer

continuous walls but wiggly lines, caused by a breaking of carbon–carbon bonds and a reduction in the atomic arrangement order. Once the inner walls at a specific region get close, a zipper-like effect, where the tube walls in the neighboring region move closer, is created and leads to a full collapse of CNT all along its length. In the process, atomic replacement is induced by the high energy electron collision with carbon atoms. **Figure 15a** shows the schematic view of CNT change under electron beam irradiation. The local damage occurs at a higher rate on planes perpendicular to the beam, causing significant damage at the top and bottom of the CNT. Meanwhile, the less damaged part of the walls tends to relax toward the equilibrium planar graphitic morphology, i.e., collapsed CNTs. Banhart et al.<sup>[84]</sup> further studied the production and migration of carbon interstitials in CNTs under electron irradiation. Figure 15b presents the structure evolution of the MWNT under electron beam. Collapse of the MWNT is accompanied by the formation of irregular graphitic cages in the hollow core. The initially cylindrical structure evolves into a morphology of a double cone. The material lost during CNT collapse is roughly the same as the aggregates making up the graphitic cages. When the shells shrink, the inner shells are successively lost, but the outer shell remains undamaged. The results indicate a relatively low stability of inner shells, which is attributed to a higher defect generation rate and/or a higher defect diffusivity in the hollow core of the tube. To gain insights in the stability of CNT shells under electron beam, the mobility barriers of adatom migration inside tube and on the surface are compared by density functional theory simulations. The barrier for atom migration inside CNT along the axis is 0.5 eV, which is much smaller than the diffusion barrier on the outer surface (1.0 eV). If a carbon atom is displaced on the outer surface of the CNT, the large energy barrier and the close separation from the vacancy would facilitate the spontaneous reannealing so that the outer layer remains undamaged. On the contrary, the escape of an adatom inside the layer along the axial direction is

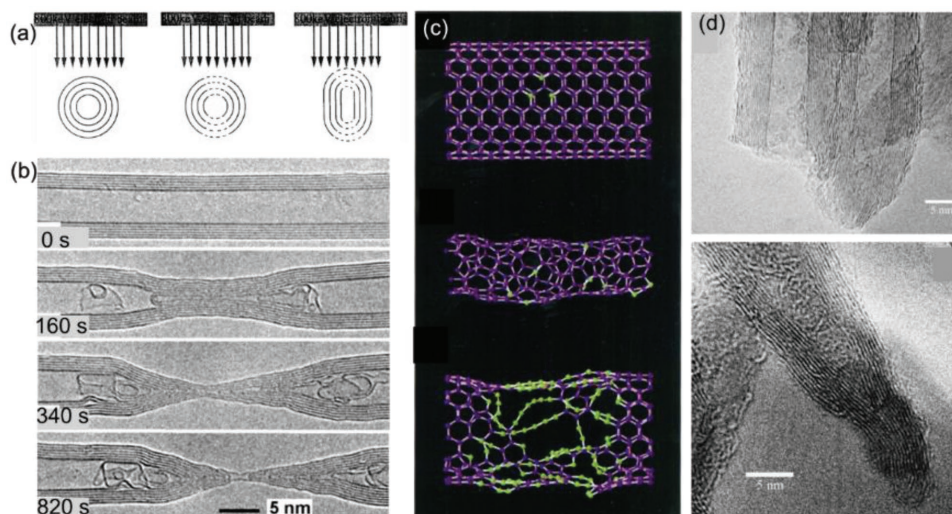


**Figure 15.** a) Schematic view of changes in CNT during electron irradiation. Reproduced with permission.<sup>[83]</sup> Copyright 1996, Elsevier B.V. b) Structure evolution of a MWNT under electron irradiation, the irradiation time is labeled in each image. Reproduced with permission.<sup>[84]</sup> Copyright 2005, American Physical Society. c) Simulation results of surface reconstruction for a SWNT. Reproduced with permission.<sup>[85]</sup> Copyright 1998, American Physical Society. d) Morphologies of CNTs after ball milling. Reproduced with permission.<sup>[86]</sup> Copyright 2004, Elsevier B.V.

avored due to the smaller energy barrier and higher mobility. Overall, the electron irradiation-induced collapse of CNTs arises from the loss of atoms inside CNTs and the diffusion of interstitials through the inner hollow along the axial direction.

The collapse of CNTs under electron irradiation is also applicable to SWNTs.<sup>[85]</sup> For  $sp^2$ -bonded carbon, knock-on atoms from the lattice could occur when electron energy is larger than 120 keV.<sup>[87]</sup> As long as irradiation persists, atom removal from the SWNT occurs and vacancies are created. The produced vacancies would cluster into large holes in the structure. Meanwhile, due to the generation of dangling bonds associated with the defects, the system becomes energetically unstable, leading to the SWNT shrinkage through atomic rearrangement (Figure 15c). In about 30 min irradiation, the original SWNT diameter of 1.4 nm shrinks to 0.4 nm. The shrinking of SWNTs also results from the loss of carbon atoms and subsequent shrinkage. Together with temperature modulation, the electron irradiation could tailor the structure of CNTs with monolayer precision, creating new carbon morphologies.<sup>[88]</sup> Consequently, the reconstruction of CNTs under electron irradiation could lead to the formation of CEGNRs, although the process is complicated.

**Ball Milling-Induced CNT Collapse:** Besides electron irradiation, ball milling also could transform CNTs into other morphologies. The treatment of CNTs by ball milling was first reported by Li et al.,<sup>[89]</sup> who milled a mixture of CNTs and iron powder to produce carbon particles. During the ball milling process, the stress applied onto CNT surface could completely break CNTs from the defective sites and generate open-ended CNTs. If only some layers rupture, small curved graphene sheets may deposit on the fractures to eliminate the dangling bonds, resulting in the closure of the carbon nanoparticles. The nearly closed ellipsoidal nanoparticles form with continued rupture and closure. Increasing the balling time transforms the configuration of carbon particle from metastable ellipsoidal shape into spherical one. During the process of ball milling, CNT collapse, at least at the end of CNTs, could be easily obtained. Kónya et al.<sup>[86]</sup> systematically investigated the end morphology of ball-milled CNTs and discussed the stability of CNTs with partially or completely collapsed open ends. Ball milling produces short CNTs with new generated tips, accompanied with the decrease of length/diameter aspect ratio. The cleavage of CNTs is induced by the stresses applied by ball milling and occurs at defective sites of CNTs, like kinks. Figure 15d presents two different types of ends of cleaved CNTs: open-ended and close-ended. For the close-ended CNTs, the innermost cylinders collapse dramatically. All the close-ended CNTs are asymmetric and converge at the end, which is important in elucidating the cleavage mechanism. In the ball milling process, the axial pressure generated could reach 2–6 GPa, which is insufficient to break defect-free CNTs but enough to break the weakest position of CNTs, like the kink area. The asymmetric feature of the ends inherits the geometry of the kink. After the breaking of CNTs along the kink site, partially collapsed CNTs could remain closed. The observation of partially collapsed CNTs with close ends might have potential applications in gas adsorption. Although only partially collapsed CNTs are observed in the work, it is possible to achieve fully collapsed CNTs if the starting CNTs have fewer wall numbers and larger inner diameters.

## 4. Conclusions and Prospects

The unique structure and configuration of CEGNRs render them extraordinary properties, including excellent mechanical properties, superior thermal conductivity, interesting electrical, optical, and magnetic properties. Therefore, CEGNRs can be potentially applied in a variety of fields, such as the FETs in nanoelectronics, energy suppliers, nanotorsional actuator, ultrastrong fibers, and thermal interface materials. The preparation of CEGNRs is the precondition to realize their potential applications. So far, several strategies have been developed to achieve CEGNRs, mostly through the collapse of CNTs. On one hand, it is possible to generate CNTs with large inner diameters, which could spontaneously collapse, leading to the formation of CEGNRs. Particularly, the efforts in determining the threshold diameter for CNT collapse are well addressed experimentally and theoretically. On the other hand, CEGNRs can be prepared by exerting external forces onto cylindrical CNTs. The forces can be exerted by hydrostatic pressure, ball milling, or electron irradiation.

Despite the progress, there are still many challenges in CEGNR field: i) to determine the  $R_{thr}(N)$  for CNTs with different wall numbers. Although previous work has addressed the  $R_{thr}$  for suspended SWNTs, the threshold diameters for bundled SWNTs and MWNTs in different forms have yet to be determined. More efforts should be made to synthesize CNTs with diameters close to  $R_{thr}(N)$  and large inner diameters; ii) large-scale production of CEGNRs. Some techniques, such as nanomanipulation and electrically unwrapping, have shown the possibility to achieve CEGNRs. However, these approaches generally suffer from low yield, inhibiting their wide application in synthesizing CEGNRs. Techniques, like CVD and solution phase extraction, could be potentially applied for bulk synthesis. Further efforts are required to improve the purity and decrease the cost of the approaches; iii) to prepare the CEGNRs with controlled width and thickness. So far, the prepared CEGNRs have wide distributions of widths and layers. Further attempts should be focused on preparing diameter and wall number controlled CNTs or graphene tubes; iv) To prepare CEGNRs with defined stacking orders. From collapse of SWNTs, GNRs with different stacking orders have been reported. However, it is one of the most challenging tasks in carbon community to control the chiral angle of CNTs with large inner diameters, which defines the final stacking orders of the CEGNRs; v) to systematically investigate the properties of CEGNRs. Limited reports have been dictated to study the mechanical and electrical properties of CEGNRs. Detailed studies on the properties of CEGNRs should be carried out on samples with different widths, layer numbers and stacking orders; vi) to explore the potential applications of CEGNRs. Due to the difficulties in manipulating the CEGNRs, the proposed applications are mainly based on theoretical predications and prototype experiments. Grounded on the progress made in CEGNR preparation, extensive experimental studies on their applications should be carried out in the future. If the challenges can be fulfilled, more breakthroughs in CEGNR-based nanoscience and nanotechnology are expected.

## Acknowledgements

The authors would also like to acknowledge the Ministry of Science and Technology of China (Grant Nos. 2016YFA0200101 and 2016YFA0200104), the National Natural Science Foundation of China (Grant Nos. 21233001, 21790052, and 51720105003). The work was also supported by the Taishan Scholar Advantage and Characteristic Discipline Team of Eco Chemical Process and Technology, the Natural Science Foundation of Shandong Province of China (Grant No. ZR2016EMM10), the Scientific Research Foundation of Shandong University of Science and Technology for Recruited Talents (Grant No. 2016RCJJ001), and the Open Funds of the State Key Laboratory (Grant No. MDPC201703). L. N. Zhang is acknowledged for help in preparing the manuscript.

## Conflict of Interest

The authors declare no conflict of interest.

## Keywords

carbon nanotube collapse, close-edged graphene nanoribbons, electronic properties, mechanical properties, threshold diameter

Received: October 26, 2018  
Revised: November 22, 2018  
Published online:

- [1] K. S. Novoselov, A. K. Geim, S. V. Morozov, D. Jiang, Y. Zhang, S. V. Dubonos, I. V. Grigorieva, A. A. Firsov, *Science* **2004**, 306, 666.
- [2] a) C. Lee, X. Wei, J. W. Kysar, J. Hone, *Science* **2008**, 321, 385; b) M. M. J. Treacy, T. W. Ebbesen, J. M. Gibson, *Nature* **1996**, 381, 678; c) A. A. Balandin, S. Ghosh, W. Bao, I. Calizo, D. Teweldebrhan, F. Miao, C. N. Lau, *Nano Lett.* **2008**, 8, 902; d) J. H. Chen, C. Jang, S. Xiao, M. Ishigami, M. S. Fuhrer, *Nat. Nanotechnol.* **2008**, 3, 206.
- [3] F. Schwierz, *Nat. Nanotechnol.* **2010**, 5, 487.
- [4] S. Y. Zhou, G. H. Gweon, A. V. Fedorov, P. N. First, W. A. de Heer, D. H. Lee, F. Guinea, A. H. Castro Neto, A. Lanzara, *Nat. Mater.* **2007**, 6, 770.
- [5] R. Balog, B. Jorgensen, L. Nilsson, M. Andersen, E. Rienks, M. Bianchi, M. Fanetti, E. Laegsgaard, A. Baraldi, S. Lizzit, Z. Sljivancanin, F. Besenbacher, B. Hammer, T. G. Pedersen, P. Hofmann, L. Hornekaer, *Nat. Mater.* **2010**, 9, 315.
- [6] a) K. P. Loh, Q. Bao, P. K. Ang, J. Yang, *J. Mater. Chem.* **2010**, 20, 2277; b) J. Son, S. Lee, S. J. Kim, B. C. Park, H. K. Lee, S. Kim, J. H. Kim, B. H. Hong, J. Hong, *Nat. Commun.* **2016**, 7, 13261; c) W. Zhang, C. T. Lin, K. K. Liu, T. Tite, C. Y. Su, C. H. Chang, Y. H. Lee, C. W. Chu, K. H. Wei, J. L. Kuo, L. J. Li, *ACS Nano* **2011**, 5, 7517.
- [7] J. Wang, R. Zhao, M. Yang, Z. Liu, *J. Chem. Phys.* **2013**, 138, 351.
- [8] a) K. Nakada, M. Fujita, G. Dresselhaus, M. S. Dresselhaus, *Phys. Rev. B* **1996**, 54, 17954; b) K. Wakabayashi, M. Fujita, H. Ajiki, M. Sigrist, *Phys. Rev. B* **1999**, 59, 8271; c) M. Y. Han, B. Ozyilmaz, Y. Zhang, P. Kim, *Phys. Rev. Lett.* **2007**, 98, 206805.
- [9] X. Wang, Y. Ouyang, X. Li, H. Wang, J. Guo, H. Dai, *Phys. Rev. Lett.* **2008**, 100, 206803.
- [10] a) H. Murayama, T. Maeda, *Nature* **1990**, 345, 791; b) R. M. Jacobberger, B. Kiraly, M. Fortin-Deschenes, P. L. Levesque, K. M. Mcelhinny, G. J. Brady, D. R. Rojas, R. S. Singha, A. Mannix, M. G. Lagally, *Nat. Commun.* **2015**, 6, 8006.
- [11] J. Baringhaus, M. Ruan, F. Edler, A. Tejeda, M. Sicot, A. Taleb-Ibrahimi, A. P. Li, Z. Jiang, E. H. Conrad, C. Berger, C. Tegenkamp, W. A. de Heer, *Nature* **2014**, 506, 349.
- [12] a) L. Jiao, L. Zhang, X. Wang, G. Diankov, H. Dai, *Nature* **2009**, 458, 877; b) D. V. Kosynkin, A. L. Higginbotham, A. Sinitskii, J. R. Lomeda, A. Dimiev, B. K. Price, J. M. Tour, *Nature* **2009**, 458, 872.
- [13] a) X. Yang, X. Dou, A. Rouhanipour, L. Zhi, H. J. Rader, K. Mullen, *J. Am. Chem. Soc.* **2008**, 130, 4216; b) J. Cai, P. Ruffieux, R. Jaafar, M. Bieri, T. Braun, S. Blankenburg, M. Muoth, A. P. Seitsonen, M. Saleh, X. Feng, K. Mullen, R. Fasel, *Nature* **2010**, 466, 470.
- [14] a) Y. W. Son, M. L. Cohen, S. G. Louie, *Nature* **2006**, 444, 347; b) P. Koskinen, S. Malola, H. Hakkinen, *Phys. Rev. Lett.* **2008**, 101, 115502; c) X. Jia, J. Camposdelgado, M. Terrones, V. Meunier, M. S. Dresselhaus, *Nanoscale* **2011**, 3, 86.
- [15] a) P. Koskinen, S. Malola, H. Häkkinen, *Phys. Rev. B* **2009**, 80, 073401; b) X. Li, X. Wang, L. Zhang, S. Lee, H. Dai, *Science* **2008**, 319, 1229; c) X. Jia, M. Hofmann, V. Meunier, B. G. Sumpter, J. Campos-Delgado, J. M. Romo-Herrera, H. Son, Y. P. Hsieh, A. Reina, J. Kong, M. Terrones, M. S. Dresselhaus, *Science* **2009**, 323, 1701.
- [16] a) N. G. Chopra, L. X. Benedict, V. H. Crespi, M. L. Cohen, S. G. Louie, A. Zettl, *Nature* **1995**, 377, 135; b) C. G. Zhang, K. Bets, S. S. Lee, Z. Z. Sun, F. Mirri, V. L. Colvin, B. I. Yakobson, J. M. Tour, R. H. Hauge, *ACS Nano* **2012**, 6, 6023; c) H. R. Barzegar, A. Yan, S. Coh, E. Gracia-Espino, C. Ojeda-Aristizabal, G. Dunn, M. L. Cohen, S. G. Louie, T. Wågberg, A. Zettl, *Nano Res.* **2017**, 10, 1942; d) M. He, J. Dong, K. Zhang, F. Ding, H. Jiang, A. Loiseau, J. Lehtonen, E. I. Kauppinen, *ACS Nano* **2014**, 8, 9657.
- [17] L. X. Benedict, N. G. Chopra, M. L. Cohen, A. Zettl, S. G. Louie, V. H. Crespi, *Chem. Phys. Lett.* **1998**, 286, 490.
- [18] C. E. Giusca, Y. Tison, S. R. P. Silva, *Nano Lett.* **2008**, 8, 3350.
- [19] a) M. Motta, A. Moisala, I. A. Kinloch, A. H. Windle, *Adv. Mater.* **2007**, 19, 3721; b) J. Kou, X. Zhou, Y. Fang, Y. Chen, H. Lu, H. Ye, F. Wu, J. Fan, *Appl. Phys. Lett.* **2013**, 102, 123902.
- [20] a) M. Terrones, A. R. Botello-Méndez, J. Campos-Delgado, F. López-Urías, Y. I. Vega-Cantú, F. J. Rodríguez-Macías, A. L. Elías, E. Munoz-Sandoval, A. G. Cano-Márquez, J.-C. Charlier, *Nano Today* **2010**, 5, 351; b) C. Mattevi, H. Kim, M. Chhowalla, *J. Mater. Chem.* **2011**, 21, 3324; c) Y. Zhang, L. Zhang, C. Zhang, *Acc. Chem. Res.* **2013**, 46, 2329; d) R. Muñoz, C. Gómez-Aleixandre, *Chem. Vap. Deposition* **2013**, 19, 297.
- [21] T. Tang, A. Jagota, C. Y. Hui, N. J. Glassmaker, *J. Appl. Phys.* **2005**, 97, 074310.
- [22] a) M. He, X. Wang, L. Zhang, Q. Wu, X. Song, A. I. Chernov, P. V. Fedotov, E. D. Obratsova, J. Sainio, H. Jiang, *Carbon* **2018**, 128, 249; b) M. He, Y. Magnin, H. Jiang, H. Amara, E. I. Kauppinen, A. Loiseau, C. Bichara, *Nanoscale* **2018**, 10, 6744; c) S. Iijima, *Nature* **1991**, 354, 56; d) M. He, S. Zhang, Q. Wu, H. Xue, B. Xin, D. Wang, J. Zhang, *Adv. Mater.* **2018**, <https://doi.org/10.1002/adma.201800805>.
- [23] J. Xiao, B. Liu, Y. Huang, J. Zuo, K. Huang, M. Yu, *Nanotechnology* **2007**, 18, 395703.
- [24] Y. Li, *Phys. Chem. Chem. Phys.* **2014**, 16, 1921.
- [25] a) V. Perebeinos, J. Tersoff, *Nano Lett.* **2014**, 14, 4376; b) X. Yuan, Y. Wang, *Nanotechnology* **2018**, 29, 075705.
- [26] C. Zhang, L. Chen, S. Chen, *Acta Mech.* **2013**, 224, 2759.
- [27] M.-F. Yu, M. J. Dyer, R. S. Ruoff, *J. Appl. Phys.* **2001**, 89, 4554.
- [28] M. F. Yu, O. Lourie, M. J. Dyer, K. Moloni, T. F. Kelly, R. S. Ruoff, *Science* **2000**, 287, 637.
- [29] X. H. Zhong, R. Wang, L. B. Liu, M. Kang, Y. Y. Wen, F. Hou, J. M. Feng, Y. L. Li, *Nanotechnology* **2012**, 23, 505712.
- [30] C. Yu, L. Shi, Z. Yao, D. Li, A. Majumdar, *Nano Lett.* **2005**, 5, 1842.
- [31] J. Al-Ghalith, H. Xu, T. Dumitrică, *Phys. Rev. Mater.* **2017**, 1, 056001.
- [32] N. Mingo, D. Broido, *Phys. Rev. Lett.* **2005**, 95, 096105.
- [33] a) M. S. Mazzoni, H. Chacham, *Appl. Phys. Lett.* **2000**, 76, 1561; b) P. E. Lammert, P. Zhang, V. H. Crespi, *Phys. Rev. Lett.* **2000**, 84, 2453; c) J.-Q. Lu, J. Wu, W. Duan, F. Liu, B.-F. Zhu, B.-L. Gu, *Phys. Rev. Lett.* **2003**, 90, 156601.

- [34] C. Gómez-Navarro, J. J. Saenz, J. Gómez-Herrero, *Phys. Rev. Lett.* **2006**, *96*, 076803.
- [35] C. Gómez-Navarro, P. J. de Pablo, J. Gómez-Herrero, *Adv. Mater.* **2004**, *16*, 549.
- [36] Y. Okuno, Y. Saito, S. Kawata, P. Verma, *Phys. Rev. Lett.* **2013**, *111*, 216101.
- [37] W. J. Yu, S. H. Chae, D. Perello, S. Y. Lee, G. H. Han, M. Yun, Y. H. Lee, *ACS Nano* **2010**, *4*, 5480.
- [38] F. Balima, S. Le Floch, C. Adessi, T. F. Cerqueira, N. Blanchard, R. Arenal, A. Brûlet, M. A. Marques, S. Botti, A. San-Miguel, *Carbon* **2016**, *106*, 64.
- [39] T. Ando, *J. Phys. Soc. Jpn.* **2017**, *86*, 064709.
- [40] X. Yang, G. Wu, *EPL* **2008**, *81*, 47003.
- [41] T. Ando, *J. Phys. Soc. Jpn.* **2017**, *86*, 024704.
- [42] R. Martel, T. Schmidt, H. Shea, T. Hertel, P. Avouris, *Appl. Phys. Lett.* **1998**, *73*, 2447.
- [43] a) T. Chang, *Phys. Rev. Lett.* **2008**, *101*, 175501; b) T. Chang, Z. Guo, *Nano Lett.* **2010**, *10*, 3490.
- [44] a) R. Senga, K. Hirahara, Y. Yamaguchi, Y. Nakayama, *J. Non-Cryst. Solids* **2012**, *358*, 2541; b) R. Senga, K. Hirahara, Y. Nakayama, *Appl. Phys. Lett.* **2012**, *100*, 083110.
- [45] H. R. Barzegar, A. Yan, S. Coh, E. Gracia-Espino, G. Dunn, T. Wägberg, S. G. Louie, M. L. Cohen, A. Zettl, *Nano Lett.* **2016**, *16*, 6787.
- [46] R. D. Downes, A. Hao, J. G. Park, Y.-F. Su, R. Liang, B. D. Jensen, E. J. Siochi, K. E. Wise, *Carbon* **2015**, *93*, 953.
- [47] H. Boehm, *Carbon* **1973**, *11*, 583.
- [48] J. Campos-Delgado, Y. Kim, T. Hayashi, A. Morelos-Gómez, M. Hofmann, H. Muramatsu, M. Endo, H. Terrones, R. Shull, M. Dresselhaus, *Chem. Phys. Lett.* **2009**, *469*, 177.
- [49] S. Lim, S.-H. Yoon, I. Mochida, J.-H. Chi, *J. Phys. Chem. B* **2004**, *108*, 1533.
- [50] J. Campos-Delgado, J. M. Romo-Herrera, X. Jia, D. A. Cullen, H. Muramatsu, Y. A. Kim, T. Hayashi, Z. Ren, D. J. Smith, Y. Okuno, *Nano Lett.* **2008**, *8*, 2773.
- [51] M. Endo, Y. Kim, T. Hayashi, T. Yanagisawa, H. Muramatsu, M. Ezaka, H. Terrones, M. Terrones, M. Dresselhaus, *Carbon* **2003**, *41*, 1941.
- [52] P. Nikolaev, A. Thess, A. G. Rinzler, D. T. Colbert, R. E. Smalley, *Chem. Phys. Lett.* **1997**, *266*, 422.
- [53] M. Terrones, H. Terrones, F. Banhart, J. Charlier, P. M. Ajayan, *Science* **2000**, *288*, 1226.
- [54] U. Kim, H. Gutierrez, J. Kim, P. Eklund, *J. Phys. Chem. B* **2005**, *109*, 23358.
- [55] M. J. López, A. Rubio, J. A. Alonso, S. Lefrant, K. Méténier, S. Bonnamy, *Phys. Rev. Lett.* **2002**, *89*, 255501.
- [56] B. Liu, M.-F. Yu, Y. Huang, *Phys. Rev. B* **2004**, *70*, 161402.
- [57] K. Yan, Q. Xue, Q. Zheng, D. Xia, H. Chen, J. Xie, *J. Phys. Chem. C* **2009**, *113*, 3120.
- [58] a) J. A. Elliott, J. K. Sandler, A. H. Windle, R. J. Young, M. S. Shaffer, *Phys. Rev. Lett.* **2004**, *92*, 095501; b) R. S. Ruoff, J. Tersoff, D. C. Lorents, S. Subramoney, B. Chan, *Nature* **1993**, *364*, 514.
- [59] G. Gao, T. Cagin, W. A. Goddard III, *Nanotechnology* **1998**, *9*, 184.
- [60] P. Zhang, V. H. Crespi, *Phys. Rev. Lett.* **1999**, *83*, 1791.
- [61] H. J. Liu, K. Cho, *Appl. Phys. Lett.* **2004**, *85*, 807.
- [62] S. Zhang, R. Khare, T. Belytschko, K. J. Hsia, S. L. Mielke, G. C. Schatz, *Phys. Rev. B* **2006**, *73*, 075423.
- [63] M. Hasegawa, K. Nishidate, *Phys. Rev. B* **2006**, *74*, 115401.
- [64] W. Lu, T.-W. Chou, B.-S. Kim, *Phys. Rev. B* **2011**, *83*, 134113.
- [65] J. Liu, *Arch. Appl. Mech.* **2012**, *82*, 767.
- [66] M. Hasegawa, K. Nishidate, N. Yoshimoto, *Phys. Rev. B* **2015**, *92*, 245429.
- [67] C. L. Cheung, A. Kurtz, H. Park, C. M. Lieber, *J. Phys. Chem. B* **2002**, *106*, 2429.
- [68] Z. J. Han, K. Ostrikov, *J. Am. Chem. Soc.* **2012**, *134*, 6018.
- [69] J. Bernholc, C. Brabec, M. Buongiorno Nardelli, A. Maiti, C. Roland, B. I. Yakobson, *Appl. Phys. A: Mater. Sci. Process.* **1998**, *67*, 39.
- [70] M. He, H. Jiang, E. I. Kauppinen, J. Lehtonen, *Nanoscale* **2012**, *4*, 7394.
- [71] C.-T. Lin, T.-H. Chen, T.-S. Chin, C.-Y. Lee, H.-T. Chiu, *Carbon* **2008**, *46*, 741.
- [72] D. Wei, Y. Liu, H. Zhang, L. Huang, B. Wu, J. Chen, G. Yu, *J. Am. Chem. Soc.* **2009**, *131*, 11147.
- [73] Y.-X. Zhang, Y. Jia, *Appl. Surf. Sci.* **2015**, *357*, 1205.
- [74] M. He, H. Amara, H. Jiang, J. Hassinen, C. Bichara, R. H. Ras, J. Lehtonen, E. I. Kauppinen, A. Loiseau, *Nanoscale* **2015**, *7*, 20284.
- [75] K. Kim, A. Sussman, A. Zettl, *ACS Nano* **2010**, *4*, 1362.
- [76] D. H. Choi, Q. Wang, Y. Azuma, Y. Majima, J. H. Warner, Y. Miyata, H. Shinohara, R. Kitaura, *Sci. Rep.* **2013**, *3*, 1617.
- [77] B. I. Yakobson, C. Brabec, J. Bernholc, *Phys. Rev. Lett.* **1996**, *76*, 2511.
- [78] S. Chesnokov, V. Nalimova, A. Rinzler, R. Smalley, J. Fischer, *Phys. Rev. Lett.* **1999**, *82*, 343.
- [79] J. Tang, L.-C. Qin, T. Sasaki, M. Yudasaka, A. Matsushita, S. Iijima, *Phys. Rev. Lett.* **2000**, *85*, 1887.
- [80] M. Peters, L. McNeil, J. P. Lu, D. Kahn, *Phys. Rev. B* **2000**, *61*, 5939.
- [81] D. Kahn, J. P. Lu, *Phys. Rev. B* **1999**, *60*, 6535.
- [82] J. Sandler, M. Shaffer, A. Windle, M. Halsall, M. Montes-Moran, C. Cooper, R. Young, *Phys. Rev. B* **2003**, *67*, 035417.
- [83] N. G. Chopra, F. Ross, A. Zettl, *Chem. Phys. Lett.* **1996**, *256*, 241.
- [84] F. Banhart, J. Li, A. Krasheninnikov, *Phys. Rev. B* **2005**, *71*, 241408.
- [85] P. Ajayan, V. Ravikumar, J.-C. Charlier, *Phys. Rev. Lett.* **1998**, *81*, 1437.
- [86] Z. Kónya, J. Zhu, K. Niesz, D. Mehn, I. Kiricsi, *Carbon* **2004**, *42*, 2001.
- [87] M. Zaiser, F. Banhart, *Phys. Rev. Lett.* **1997**, *79*, 3680.
- [88] J. Li, F. Banhart, *Nano Lett.* **2004**, *4*, 1143.
- [89] Y. Li, B. Wei, J. Liang, Q. Yu, D. Wu, *Carbon* **1999**, *37*, 493.